Journal of the Mechanics and Physics of Solids 121 (2018) 258–280

Contents lists available at ScienceDirect

Journal of the Mechanics and Physics of Solids

journal homepage: www.elsevier.com/locate/jmps

Corrosive fracture of electrodes in Li-ion batteries

Rong Xu, Kejie Zhao*

School of Mechanical Engineering, Purdue University, West Lafayette, IN 47907, USA

ARTICLE INFO

Article history:
Received 27 June 2018
Revised 27 July 2018
Accepted 27 July 2018
Available online 2 August 2018

Keywords:
Fracture
Diffusion
Corrosion
Chemomechanics
Li-ion batteries

ABSTRACT

Fracture in electrochemical systems is often corrosive in nature. In Li-ion batteries, Li reaction causes embrittlement of the host material and typically results in a decrease of fracture toughness of anodes when Li inserts and a reduction of fracture toughness of cathodes when Li extracts. The dynamics of crack growth depends on the chemomechanical load, kinetics of Li transport, and the Li embrittlement effect. We implement a theory of coupled diffusion, large deformation, and crack growth into finite element modeling and simulate the corrosive fracture of electrodes under concurrent mechanical and chemical load. We construct the phase diagram delineating the unstable, arrested, and delayed fracture zones. We examine in detail the competition between energy release rate and fracture resistance as crack grows during both Li insertion and extraction. The wait-and-go behavior in the delayed fracture zone relies on the chemomechanical load and the supply of Li to the crack tip. We apply the theory to model the intergranular fracture in $LiNi_xMn_yCo_zO_2$ (NMC) particles which is the major mechanical degradation of the cathode material. The structural decohesion is induced by the mismatch strain at the grain boundaries. The evolving interfacial strength at different states of charge and different cycle numbers measured by in-situ nanoindentation is implemented in the numerical simulation. We model the corrosive behavior of intergranular cracks in NMC upon Li cycles and compare the crack morphologies with experiments.

1. Introduction

Mechanical degradation upon ion reactions in redox active materials is a prevalent issue causing impedance growth and performance fade in the state-of-the-art Li-ion batteries and solid-state batteries (Tarascon and Armand, 2012; Palacin and de Guibert, 2016; Zhang et al., 2017b). When Li is intercalating into the host material, electrodes deform with a characteristic volumetric strain ranging from a few percent in intercalation-type electrodes to a few hundred percent in conversion- or insertion-type materials (Xu et al., 2016). Fracture is a consequence of the repetitive deformation and contributes to a major mechanism of aging in a wide spectrum of materials over cycles, (Zhang et al., 2007; McDowell et al., 2016; Xu and Zhao, 2016a; Zhao and Cui, 2016; Zhang, 2017), including fracture of the redox active materials (Wang et al., 1999; Liu et al., 2012; Mu et al., 2018), crack of inactive conductive matrix (Ning et al., 2003), debonding of composite films from the current collector (Maranchi et al., 2006), shedding of the solid electrolyte interface (SEI) (Sun et al., 2014), and structural disintegration of aggregated particles (Kim et al., 2016; Xu et al., 2017b; Ryu et al., 2018) in both anode and cathode. Mechanical degradation and the constant disruption of the solid interfaces result in Li depletion, increase of the ohmic and thermal resistance,

* Corresponding author.
E-mail address: kjzhao@purdue.edu (K. Zhao).

https://doi.org/10.1016/j.jmps.2018.07.021
0022-5096/

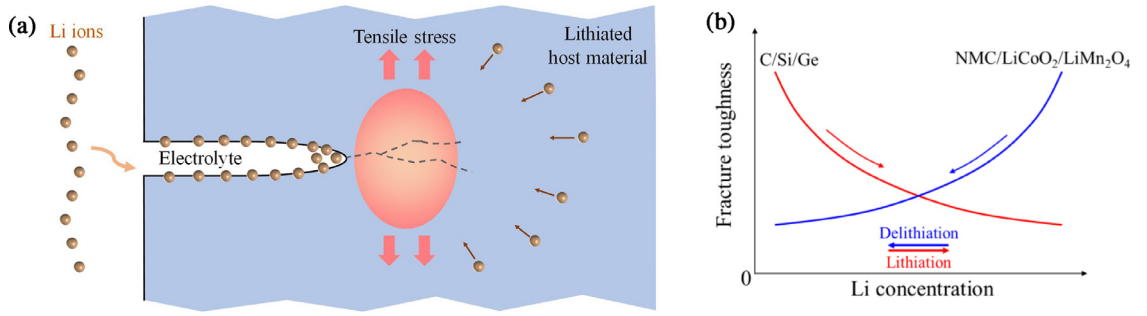

Fig. 1. (a) Schematic of corrosive fracture of electrodes in Li-ion batteries. Li diffuses rapidly on the crack surface and accumulates at the crack tip. Li reaction causes embrittlement of the host material and growth of the crack. (b) Sketch of experimental observations of Li embrittlement in active anode and cathode materials. Fracture toughness of anode materials usually decreases upon Li insertion while fracture toughness of cathodes decreases during Li extraction.

and steady fade of the cyclic efficiency, while the isolation of the active materials from the conductive network causes a mostly immediate loss of capacity of batteries.

Fracture is an overwhelming issue in electrodes of intrinsically large deformation associated with Li reactions (Liu et al., 2012; Lee et al., 2015). The formation of extensive cracks in the early state of the electrochemical reactions causes catastrophic failure of batteries. Limited success so far has been achieved to mitigate such mechanical degradation in high-capacity electrodes (McDowell et al., 2016; Zhang, 2017; Zhang et al., 2017b). Less recognized is mechanical failure in electrodes of relatively small volumetric deformation ($<10\%$) such as $LiNi_xMn_yCo_zO_2$ (NMC, $x+y+z=1$), $LiCoO_2$ and $LiMn_2O_4$ cathode (Wang et al., 1999; Hao et al., 2014; Xu et al., 2017b; Ryu et al., 2018). Mechanical stresses in the small-volumetric-change materials also induce extensive materials defects including dislocations (Yan et al., 2017), cavitation (Kim et al., 2016), intragranular and intergranular cracks (Mu et al., 2018). There have been tremendous efforts to analyze and predict fracture of electrodes caused by diffusion-induced stresses (Huggins and Nix, 2000; Christensen and Newman, 2006; Bhandakkar and Gao, 2010; Woodford et al., 2010; Zhao et al., 2010; Ryu et al., 2011; Zhao et al., 2012; Xu et al., 2016). Most of the early studies focus on the fracture analysis using either a stress criterion (Christensen and Newman, 2006; Zhang et al., 2007) or the Griffith fracture mechanics (Huggins and Nix, 2000; Zhao et al., 2010; Zhao et al., 2012; Jia and Liu, 2016) to predict the onset of crack. It has been revealed that the particle size and the charging rate significantly influence the fracture behavior of electrodes which was soon confirmed by several experiments (Chan et al., 2008; Liu et al., 2012; Lee et al., 2015). The later development of continuum theories of coupled diffusion and finite deformation allows to examine the close interactions between the diffusion kinetics and mechanical stresses in batteries and to explore the dynamics of crack growth coupled with Li transport near the crack tip. (Bower et al., 2011; Brassart et al., 2013; Bower et al., 2015; Xu and Zhao, 2016b).

Fracture in electrochemical systems is often corrosive in nature. Corrosive fracture is also known variously in the mechanics community as environment-sensitive fracture, subcritical crack growth, or stress-corrosion cracking, which differs from the conventional sense of corrosion in electrochemistry. In Li-ion batteries, mechanical stresses regulate Li diffusion and the crack propagation is tightly coupled with the redistribution of Li. Fig. 1(a) sketches the interactions between the stress field at the crack tip and the Li profile. The chemical load is applied by supplying a field of Li concentration or Li flux. Li diffuses rapidly along the crack path because of the high surface diffusivity and accumulates at the crack tip because of the stress concentration ahead of the crack. This phenomenon is analogous to the diffusion of hydrogen and oxygen in fractured metals where the solute is trapped ahead of the crack tip (Sofronis and McMeeking, 1989; Alam and Das, 2009; Yang et al., 2011). Li accumulation appends an extra lithiation-induced dilatational strain at the crack tip which reduces the stress field and the driving force for crack growth. This shielding effect caused by Li accumulation is a reminiscence of crack shielding in the stress-induced martensitic transformation in ceramics (Evans, 1984). Prior studies have elaborated in detail the intimate relation between the crack driving force and Li redistribution at crack tip (Yang et al., 2011; Gao and Zhou, 2013; Haftbaradaran and Qu, 2014; Klinsmann et al., 2016b). Li redistribution does not only modulate the stress field around the crack tip, but also alter the fracture toughness of the host material, which results in a competition between the driving force and the resistance of fracture upon Li reactions. While many studies have investigated the dependence of mechanical properties of electrodes on Li composition, such as elastic modulus and hardness at different states of charge (Berla et al., 2015; Vasconcelos et al., 2017), fracture toughness is relatively less explored. A few recent novel experiments are developed to determine the evolution of fracture toughness upon Li reactions (Pharr et al., 2013; Swallow et al., 2014; Xu et al., 2017a). Fig. 1(b) illustrates the experimental observations of fracture toughness for a variety of active materials as a function of Li concentration. Li reactions cause embrittlement of the host material. In anodes, such as the alloying-type materials C, Si and Ge, fracture toughness generally decreases during Li inserts (Liu et al., 2011; Pharr et al., 2013; Pharr et al., 2016). The lithiation induced embrittlement is mainly due to the atomic bond breakage of the host materials upon Li insertion and the formation of weaker bonds between Li and the host atom which deteriorate the mechanical strength (Huang et al., 2013; Yang et al., 2013). In cathodes, such as the intercalation-type materials NMC, $LiCoO_2$ and $LiMn_2O_4$, frac-

ture toughness usually reduces upon Li extraction (Swallow et al., 2014; Mughal et al., 2016; Xu et al., 2017a). The loss of fracture resistance upon delithiation is likely due to (i) the depolarization of the transition metals (TM)-oxygen ionic bonding when Li extracts, (ii) the Jahn-Teller (JT) distortion when the transition metals transit from JT-inactive to JT-active states during delithiation, (iii) the structural destabilization caused by cation mixing in which TM ions of a similar size of Li^+ occupy the vacant Li sites (Yan et al., 2015), and (iv) the formation of nano-sized voids within the electrodes resulted from the volumetric contraction during Li extraction (Kim et al., 2016). The generation of material defects does not necessarily cause macroscopic damage, however, the population and evolution of the defects will weaken the fracture toughness of the redox materials. Overall, the fracture behavior of electrodes is a result of the interactions among the Li transport, the electrochemical conditions, the stress field, and the Li embrittlement effect. Whether the stress-diffusion coupling facilitates or suppresses fracture growth depends on the type of materials as well as the chemomechanical load conditions. This scenario shares similar features of corrosive fracture of metals assisted by oxygen or moisture (Molins et al., 1997; Barnoush and Vehoff, 2010). However, different from oxygen, Li might be a more corrosive species because the formation of oxides at the crack tip may shield further oxygen transport and protect unstable crack propagation, while lithiated active materials do not usually have such an effect (Cui et al., 2016).

The goal of this paper is to study the corrosive fracture of electrodes under concurrent mechanical and chemical load. We implement the continuum theory of coupled diffusion and large deformation into finite element modeling and investigate the fracture behavior that is determined by diffusion kinetics and Li embrittlement effect. We examine in detail the competition between energy release rate and fracture resistance as crack grows during both Li insertion and extraction. We construct the phase diagram delineating the unstable, arrested, and delayed fracture zones in the variable space of material properties and the load conditions. We apply the theory to model the intergranular fracture in NMC aggregated particles which constitutes the major mechanical degradation of the state-of-the-art cathode material for vehicle applications. The structural decohesion is induced by the mismatch strain at the grain boundaries. The evolving interfacial strength at different states of charge and different cycle numbers measured by our in-situ nanoindentation is implemented in the numerical simulation. We model the corrosive behavior of intergranular cracks in NMC during delithiation as well as upon Li cycles and compare the crack morphologies with experiments. We organize the paper as follows. Section 2 summarizes the governing equations for the kinematics of an elastic solid and the kinetic of Li transport in a chemomechanical system under both mechanical and chemical load. A theory based on linear elastic fracture mechanics (LEFM) is employed to determine the energy release rate of crack growth and variation of the fracture toughness due to the evolution of the chemical composition. We use a cohesive zone model (CZM) to model the crack propagation and Li transport coupled with crack generation. Section 3 presents the numerical modeling of corrosive fracture of electrodes under concurrent mechanical load and chemical (de)lithiation. We compare the evolutions of the energy release rate and material fracture toughness as the Li reaction proceeds and crack grows. We construct the phase diagrams that delineate the unstable, arrested, and delayed fracture zones in the plane spanned by the chemical load condition and the fracture toughness. We evaluate the effects of the stress regulated Li diffusion and Li insertion induced material embrittlement on the fracture behavior. We finally apply the theory to model the corrosive intergranular fracture in NMC particles. We consider the evolving interfacial strength at different states of charge and different cycles, and compare the numerical results with the recent experimental observations.

2. Theory and computation framework

2.1. Kinematics of deformation

When a solid deforms by mechanical forces under constraint conditions, each material particle retains its material coordinates $\mathbf{X}$ and its spatial coordinates $\mathbf{x}$ are determined by the displacement vector $\mathbf{u}(\mathbf{X}, t)$, pointing from the reference position to the current configuration,

$$\mathbf{x}(\mathbf{X}, t) = \mathbf{X} + \mathbf{u}(\mathbf{X}, t) \ . \tag{1}$$

The deformation gradient $\mathbf{F}$ includes the complete information about the local strain and rotation of the material. $\mathbf{F}$ can be written in terms of the displacement gradient,

$$\mathbf{F} = \frac{\partial \mathbf{x}}{\partial \mathbf{X}} = \nabla \mathbf{u} + \mathbf{I} \ . \tag{2}$$

We use a theory of the multiplicative decomposition of the deformation gradient,

$$\mathbf{F} = \mathbf{F}_{\text{el}} \mathbf{F}_{\text{inel}}, \tag{3}$$

where $\mathbf{F}_{\text{el}}$ represents the reversible elastic deformation and $\mathbf{F}_{\text{inel}}$ represents the inelastic distortion of the material. The ratio of the current to the initial volume (or mass density) is given by

$$\frac{\partial V}{\partial V_0} = \det(\mathbf{F}) = J > 0, \tag{4}$$

and hence

$$J = J_{\text{el}} \, J_{\text{inel}}, \ J_{\text{el}} = \det(\mathbf{F}_{\text{el}}) > 0, \ J_{\text{inel}} = \det(\mathbf{F}_{\text{inel}}) > 0. \tag{5}$$

The inelastic deformation can be further decomposed into two parts: a volumetric change caused by Li insertion or extraction, and plastic deformation of the material due to the irreversible shape change. For small-volumetric-change electrodes such as layered NMC, we may ignore the plastic contribution,

$$\mathbf{F}_{\text{inel}} = \mathbf{F}_{\text{Li}}, \tag{6}$$

where $\mathbf{F}_{\text{Li}}$ represents the eigen deformation induced by the insertion or extraction of Li into the host material. Let J_{Li} denotes the volume change per unit reference volume, we assume that this change is entirely due to the change of Li concentration in the host frame, so that the volumetric change is written as follows

$$J_{\text{Li}} = \det(\mathbf{F}_{\text{Li}}) = (1 + \Omega C), \tag{7}$$

where Ω is the partial molar volume of Li atom in the host material and $C(\mathbf{X}, t)$ is the number of Li atoms per unit volume in the reference state (i.e. nominal Li concentration). We obtain the Li insertion-induced linear deformation gradient

$$\mathbf{F}_{\text{Li}} = {J_{\text{Li}}}^{1/3}\mathbf{I} = (1 + \Omega C)^{1/3}\mathbf{I}, \tag{8}$$

Here we have assumed an isotropic expansion in each direction upon Li reactions. This assumption is not necessarily correct, for instance, in the layered cathode, the deformation is highly anisotropic. We will consider anisotropic deformation when we apply the theory in the later modeling of NMC aggregated particles.

The stress tensor satisfies the mechanical equilibrium condition,

$$\nabla \cdot \mathbf{P} + \mathbf{B}_{\text{v}} = \mathbf{0}, \tag{9}$$

where $\mathbf{P}$ represents the first Piola-Kirchhoff (PK) stress that relates forces in the current configuration with respect to the area in the reference configuration (nominal stress). The volume force vector $\mathbf{B}_{\text{v}}$ is also determined with respect to the reference volume, and the tensor divergence operator ∇ is computed in the Lagrangian (reference) coordinates. The first PK stress $\mathbf{P}$ is calculated from the second PK stress as

$$\mathbf{P} = \mathbf{FS}, \tag{10}$$

where $\mathbf{S}$ represents the second PK stress where both force and area are represented in the reference configuration. $\mathbf{S}$ is related to the symmetric Cauchy stress $\boldsymbol{\sigma}$ in the deformed body by

$$\boldsymbol{\sigma} = J^{-1}\mathbf{FSF}^{\text{T}} . \tag{11}$$

It would be convenient to introduce the elastic second PK Stress (Anand, 2012),

$$\mathbf{S}_{\text{el}} = J_{\text{el}}\mathbf{F}_{\text{el}}^{-1}\sigma\mathbf{F}_{\text{el}}^{-\text{T}} . \tag{12}$$

We adopt the constitutive model proposed in the prior work (Bower et al., 2011; Anand, 2012). The elastic second PK stress is related to the elastic Green–Lagrange strain tensor $\mathbf{E}_{\text{el}}$ by

$$\mathbf{S}_{\text{el}} = J_{\text{el}}\mathbf{F}_{\text{el}}^{-1}\sigma\mathbf{F}_{\text{el}}^{-\text{T}} = \mathbf{C} : \mathbf{E}_{\text{el}}, \tag{13}$$

where $\mathbf{C}$ is the elastic constant matrix for the material in the reference configuration. The elastic Green-Lagrange strain tensor is computed from the elastic right Cauchy-Green deformation tensor

$$\mathbf{E}_{\text{el}} = (\mathbf{C}_{\text{el}} - \mathbf{I})/\mathbf{2}, \tag{14}$$

where the elastic right Cauchy-Green deformation tensor is determined by

$$\mathbf{C}_{\text{el}} = \mathbf{F}_{\text{el}}^{\text{T}}\mathbf{F}_{\text{el}} . \tag{15}$$

The governing equations for the kinematics of deformation is nonlinear. We rewrite their weak formulations and integrate into the finite element program within a Lagrangian setting. The coupled equations for mechanical equilibrium and Li diffusion will be solved simultaneously at every time step. The weak form for the mechanical equilibrium is obtained by multiplying Eq. (9) by a test function and integrating it over the volume of the material

$$\int_{V_0} (\nabla \cdot \mathbf{P} + \mathbf{B}_{\text{v}}) \cdot \text{v} dV_0 = 0, \tag{16}$$

where $\mathbf{v}(\mathbf{X}, t)$ is a test function that vanishes on the boundary. Integrating the equation by parts gives

$$\int_{V_0} \mathbf{P} : \nabla \text{v} dV_0 - \int_{V_0} \mathbf{B}_{\text{v}} \cdot \text{v} dV_0 - \int_{A_0} \mathbf{T} \cdot \text{v} dA_0 = 0, \tag{17}$$

where $\mathbf{T}$ represents the nominal surface traction that is related to the first PK stress via the formula $\mathbf{T} = \mathbf{P} \cdot \mathbf{N}_0$, where the normal vector $\mathbf{N}_0$ corresponds to the undeformed surface element.

2.2. Kinetic of diffusion

The mass conservation requires

$$\frac{\partial C}{\partial t} + \nabla \cdot \boldsymbol{J} = 0, \tag{18}$$

where $\boldsymbol{J}(\mathbf{X}, t)$ is the number of the Li atom per unit time crossing a unit area in the reference state (i.e. nominal Li flux). We adopt Fick's law to describe the kinetics of Li atoms diffusing in the host material,

$$\boldsymbol{j} = -\frac{cD}{kT}\nabla_{\mathbf{x}}\mu, \tag{19}$$

where $c(\mathbf{X}, t)$ is the number of Li atoms per unit volume in the current state (i.e. true concentration), $\boldsymbol{j}(\mathbf{X}, t)$ is the number of Li atoms per unit time crossing a unit area in the current state (i.e. true flux), and $\mu(\mathbf{X}, t)$ represents Li chemical potential in the host material. D, k, and T are Li diffusivity, the gas constant, and temperature, respectively. Here we assume that the Li diffusivity in the host is isotropic and is independent of the deformation gradient $\mathbf{F}$ and Li concentration C.

Eq. (19) describes Li diffusion in the current state (Eulerian coordinate) such that the quantities are written in terms of the true form and $\nabla_{\mathbf{x}}$ represents the gradient with respect to the Eulerian coordinate on the spatial frame. Using the standard transformation rules of continuum mechanics, the relationship between the nominal flux $\boldsymbol{J}$ and true flux $\boldsymbol{j}$ can be obtained. Nanson derived the formula for a material element of normal vector $\mathbf{N}_0$ and area dA in the reference state that deforms to a configuration of $\mathbf{n}_0$ and da in the current state

$$\mathbf{F}^{\mathrm{T}}\mathbf{n}_0 da = \det(\mathbf{F})\mathbf{N}_0 dA. \tag{20}$$

Note that the rate of Li diffusion should be independent of the description system, thus, the following condition must hold

$$\boldsymbol{j} \cdot \mathbf{n}_0 da = \boldsymbol{J} \cdot \mathbf{N}_0 dA. \tag{21}$$

Combining Eqs. (20) and (21), we obtain the relationship between the flux vectors in the two coordinates,

$$\boldsymbol{j} = \frac{\mathrm{F}}{\det(\mathbf{F})}\boldsymbol{J}\,. \tag{22}$$

The true concentration c relates to the nominal concentration C as

$$c = \frac{C}{\det(\mathbf{F})}. \tag{23}$$

Using the chain rule of partial derivatives, we obtain that

$$\nabla_{\mathbf{x}}() = \mathbf{F}^{-\mathrm{T}}\nabla(). \tag{24}$$

Combining Eqs. (20)–(24), the relationship between the nominal flux and the chemical potential in the Lagrangian frame can be written as

$$\boldsymbol{J} = -\frac{CD}{kT}\mathbf{F}^{-1}\mathbf{F}^{-\mathrm{T}}\nabla\mu. \tag{25}$$

We assume that the Helmholtz free energy per unit reference volume $\phi(\mathbf{F}, C)$ is a function of the deformation gradient and the nominal Li concentration. Derived from the thermodynamic imbalance, the chemical potential of Li can be expressed as (Bower and Guduru, 2012)

$$\mu = \frac{\partial \phi(\mathbf{F}, C)}{\partial C} - \Omega\sigma_m, \tag{26}$$

where $\sigma_m = (\sigma_1 + \sigma_2 + \sigma_3)/3$ is the mean stress. $\frac{\partial \phi(\mathbf{F}, C)}{\partial C}$ represents the isothermal chemical potential of Li at zero stress state. We assume that the elastic strains are small compared to the Li-induced deformation, and neglect the dependence of elastic moduli on Li concentration. The free energy is adopted from a prior work (Zhao et al., 2011),

$$\phi(\mathbf{F}, C) = \phi_0(C) + W(\mathbf{F}), \tag{27}$$

where $\phi_0(C)$ and $W(\mathbf{F})$ are the free energies contributed by the stress-free chemical potential and the strain energy, respectively. In a simplified form, we adopt the stress-free chemical potential of diffusing species into an ideal solid solution, originally proposed by (Larché and Cahn, 1985) and subsequently used by others (Bohn et al., 2013),

$$\frac{\partial \phi_0(C)}{\partial C} = \mu_0 + kT\ln\left(\frac{C}{C_{\max} - C}\right), \tag{28}$$

where $C_{\max}$ is the maximum Li concentration in the reference state and the constant μ_0 is a reference chemical potential. Combining Eqs. (26)–(28), the chemical potential is written as follows,

$$\mu = \mu_0 + kT\ln\left(\frac{C}{C_{\max} - C}\right) - \Omega\sigma_m, \tag{29}$$

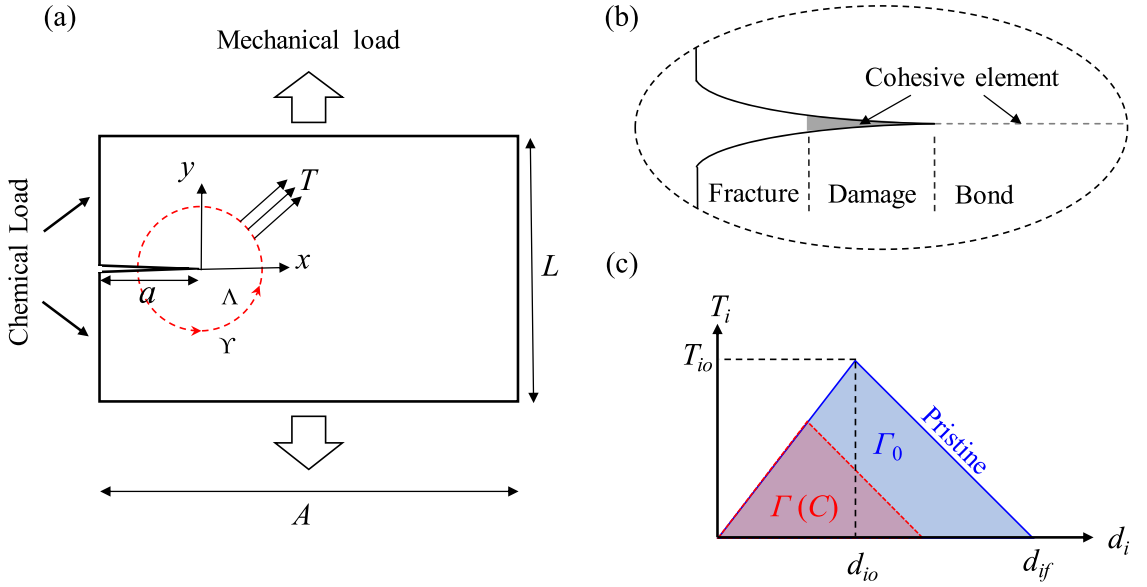

Fig. 2. (a) A model subject to the concurrent chemical and mechanical load. The red dashed circle represents the contour ϒ for calculating the energy release rate. (b) Schematic of the cohesive zone model (CZM) for simulating the crack growth in the chemomechanical system. (c) the (de)lithiation-dependent constitute law of the cohesive element. (For interpretation of the references to color in this figure legend, the reader is referred to the web version of this article.)

In writing the weak formula, we use the chemical potential $\mu(\mathbf{X},t)$ as the field variable. Following a similar procedure in Eqs. (16) and (17), the weak form for the mass transport is obtained as follows,

$$\int_{V_0}\left(\frac{\partial C}{\partial t}+\nabla\cdot\mathbf{J}\right)\hat{\mu}dV_0=0, \tag{30}$$

where $\hat{\mu}(\mathbf{X},t)$ is a test function. Integrating the equation by parts, it yields

$$\int_{V_0}\frac{\partial C}{\partial t}\hat{\mu}dV_0-\int_{V_0}\mathbf{J}\cdot\nabla\hat{\mu}dV_0+\int_{A_0}(\mathbf{J}\cdot\mathbf{N}_0)\hat{\mu}dA_0=0, \tag{31}$$

where $\mathbf{J}\cdot\mathbf{N}_0=\mathbf{J}_0$ is the nominal Li influx into the host material.

2.3. Energy release rate

In Griffith fracture mechanics, the *J*-integral is a convenient way to calculate the energy release rate *G* for linear elastic materials or materials of small-scale yielding at the crack tip. Consider an arbitrary counterclockwise path around the crack tip ϒ, Fig. 2(a), the two-dimensional path-independent *J*-integral is defined as (Rice, 1968)

$$J=\int_{\Upsilon}\left(WdX_2-\mathbf{T}\cdot\frac{\partial\mathbf{u}}{\partial X_1}ds\right), \tag{32}$$

where *W* is the strain energy density, **T** is the traction vector on the contour Υ of the outward normal $\mathbf{N}_0$. *ds* is an element length along ϒ, and X_1 and X_2 are the coordination directions.

In an electrochemical system with solid state diffusion, prior work (Gao and Zhou, 2013; Haftbaradaran and Qu, 2014; Zhang et al., 2017a) proved that the conventional *J*-integral is no longer path-independent. Recall that the *J*-integral includes the total energy within the closed contour and the energy passing through the contour line. When diffusion is involved in the system, the free energy within the contour around the crack tip will not only include the elastic strain energy but also contains the energy associated with solute diffusion and distribution. Furthermore, both mechanical work done by tractions and free energy conveyed by solid state diffusion should be accounted in the energy along the contour line. Here we utilize a modified *J*-integral proposed in the earlier work (Gao and Zhou, 2013),

$$\mathbf{J}=\int_{\Upsilon}\left(\phi dX_2-\mathbf{T}\cdot\frac{\partial\mathbf{u}}{\partial X_1}ds\right)-\int_{\Lambda}\mu\cdot\frac{\partial C}{\partial X_1}d\Lambda, \tag{33}$$

where ∧ is the area enclosed by the contour ϒ. The first line integral accounts for the total energy inside the closed contour, the second line integral represents the mechanical work done by the tractions passing through the contour line, and the

area integral represents the change of free energy within the area of the contour Υ which is equal to the energy conveyed by solid state diffusion. With the definition of chemical potential μ and free energy ϕ in Eq. (27), Eq. (33) is recast into the following form via Green's theorem,

$$\boldsymbol{J} = \int_{\Upsilon} \left(W dX_2 - \mathbf{T} \cdot \frac{\partial \mathbf{u}}{\partial X_1} ds \right) + \int_{\Lambda} (\Omega \sigma_m) \frac{\partial C}{\partial X_1} d\Lambda. \tag{34}$$

Eq. (34) is path-independent in the chemomechanical system involving both Li diffusion and mechanical deformation, and can be used to evaluate energy release rate G for crack growth. It should be noted that the simplified form Eq. (34) includes the assumption that the volumetric change due to elastic deformation is small and the elastic constants are independent on the Li composition. Gao and Zhou (2013) have evaluated the effect of these two factors in their prior work. We implement Eq. (34) into our numerical simulation using the energy domain integral method originally proposed by (Shih et al., 1986) and subsequently elaborated by (Gao and Zhou, 2013). The detail of the numerical implementation can be found in the earlier paper (Gao and Zhou, 2013).

2.4. Dynamics of crack growth

For a chemomechanical system under both mechanical and chemical load, Li profile and the stress field dynamically evolve due to the stress-diffusion coupling. Li diffusion is usually much slower than mechanical equilibrium such that the system is not always in the chemical equilibrium state especially during the crack growth. Here we simulate the dynamic stress evolution and Li diffusion coupled with crack propagation using a standard cohesive zone model (CZM) which permits the material planes in potential fracture zones to separate using a pre-defined traction–separation law (Elices et al., 2002; Roe and Siegmund, 2003). We assume that the preexisting crack propagates along its crack plane without any deflection. Therefore, cohesive elements are assigned in front of the initial crack along the path of potential crack propagation, Fig. 2(b). The history-dependent traction–separation relation of the cohesive element is plotted in Fig. 2(c). In the undamaged state, the cohesive element is linearly elastic, thus, the traction T_i in the reference state is computed from the effective gap d_i as

$$T_i = K_i d_i, \tag{35}$$

where subscript i takes the values I and II, which represent the traction responses along two directions, that are, stretching in the normal direction, mode I, and shear in the tangential direction, mode II. K_i is the stiffness of the cohesive element along the two directions which relates to the elastic modulus and shear modulus of the host material.

Damage occurs when the maximum traction exceeds the interfacial strength of the material. As shown in Fig. 2(c), the failure initiation displacement d_{i0} is determined from the maximum traction and the elastic stiffness as

$$d_{i0} = \frac{T_{i0}}{K_i}. \tag{36}$$

In general, the fracture mode is a combination of tension and shear, so the traction–separation relation for two modes must be combined into a multiaxial behavior. In this work, we define the mixed mode displacement d_m as a weighted combination of the normal gap d_I and the tangential slide d_{II}

$$d_m = \sqrt{\langle d_I \rangle^2 + {d_{II}}^2} \tag{37}$$

where $\langle\rangle$ is the MacAuley bracket defined as $\langle d_I \rangle = d_I$ for $d_I > 0$ (opening) and $\langle d_I \rangle = 0$ otherwise. We adopt the Hashin-Rotem criterion for the damage initiation (Hashin and Rotem, 1973),

$$\left(\frac{\langle T_I \rangle}{T_{I0}} \right)^2 + \left(\frac{T_{II}}{T_{II0}} \right)^2 = 1. \tag{38}$$

Combining Eqs. (35)–(37), we obtain the mixed mode failure initiation displacement

$$d_{m0} = d_{I0} d_{II0} \sqrt{\frac{{d_m}^2}{\langle d_I \rangle^2 {d_{II0}}^2 + {d_{II}}^2 {d_{I0}}^2}}. \tag{39}$$

A damage is assumed to occur when $d_m > d_{m0}$ and the stiffness is subsequently reduced even on the unloading state. Therefore, in the damaged state, Eq. (35) is rewritten as

$$T_i = (1 - D) K_i d_i \tag{40}$$

where D is a function used to describe the state of damage, which evolves from 0 to 1 based on a damage evolution criterion. We select the power law criterion here for the final failure

$$\left(\frac{G_I}{\Gamma_I} \right)^{\eta} + \left(\frac{G_{II}}{\Gamma_{II}} \right)^{\eta} = 1, \tag{41}$$

where the exponent η is called the mode mixity exponent. G_i and Γ_i are the energy release rate and fracture toughness for i mode, respectively.

For the linear separation law shown in Fig. 2(c), the failure displacement d_{if} for each mode is determined from the given fracture toughness (the area under traction–separation curve),

$$d_{if} = \frac{2\Gamma_i}{T_{i0}}, \tag{42}$$

Combining Eqs. (35)–(37) and (42), we obtain the total failure displacement in the mixed mode d_{mf} as

$$\begin{cases} d_{mf} = \frac{2\left(1+(d_{II}/d_I)^2\right)}{d_{m0}} \left(\left(\frac{K_I}{\Gamma_I}\right)^{\eta} + \left(\frac{(d_{II}/d_I)^2 K_{II}}{\Gamma_{II}}\right)^{\eta} \right)^{-\frac{1}{\eta}} & d_I > 0 \\ d_{mf} = d_{IIf} & d_I \le 0 \end{cases} \tag{43}$$

The traction reduces to zero and meanwhile new crack surfaces form when $d_m > d_{mf}$. The damage function can be described as

$$D = \min\left(1,\ \max\left(0, \frac{d_{mf}}{d_m}\left(\frac{d_m - d_{m0}}{d_{mf} - d_{m0}}\right)\right)\right). \tag{44}$$

In this work, we set the mode mixity exponent $\eta = 1$ such that the power law failure criterion in Eq. (41) is reduced to $G_I/\Gamma_I + G_{II}/\Gamma_{II} = 1$. If we ignore the shear induced damage in the host material, the failure criterion can be further reduced to $G_I = \Gamma_I$. This reduced criterion is the same with the Griffith criterion in linear fracture mechanics. Under this circumstance, we can use the CZM to simulate the dynamic co-evolution of Li distribution and the stress field in the chemomechanical system under mechanical and chemical load, and also can verify the fracture analysis based on Griffith fracture mechanics in Section 2.3. The details will be presented in the Section 3.

In the earlier section, we present that the fracture toughness of electrodes is largely dependent on Li composition, therefore, the traction-separation relation of the cohesive element should be a function of the Li concentration. Here we set the pristine fracture toughness as Γ_0 and the fracture toughness of lithiated (delithiated) state as $\Gamma(C)$. According to the two types of Li embrittlement effects shown in Fig. 1(b), the expression $\Gamma(C)$ can be written in the following form based on the recent experimental measurements (Xu et al., 2017a),

$$\begin{cases} \Gamma(C)/\Gamma_0 = 0.9(1 - C/C_{\max})^n + 0.1 & \text{Lithiation embrittlement} \\ \Gamma(C)/\Gamma_0 = 0.9(C/C_{\max})^n + 0.1 & \text{Delithiation embrittlement} \end{cases} \tag{45}$$

where n is the exponent denoting the degree of the Li-assisted embrittlement. Higher n indicates severer embrittlement effect due to the Li reaction. The first formula in Eq. (45) represents the Li insertion induced embrittlement of anode materials, such as graphite and carbon nanomaterials. The normalized Li concentration $C/C_{\max}$ varies from 0 to 1, altering the fracture toughness of active material $\Gamma(C)$ from Γ_0 to $0.1\Gamma_0$. Similarly, the second formula in Eq. (45) represents the Li extraction induced embrittlement of cathode materials upon Li extraction, such as $LiCoO_2$ and NMC. The normalized Li concentration $C/C_{\max}$ varies from 1 to 0 and alter the fracture toughness $\Gamma(C)$ from Γ_0 to $0.1\Gamma_0$. The ranges of the variation of fracture toughness upon lithiation or delithiation agree well with the experiment results (Liu et al., 2011; Swallow et al., 2014; Xu et al., 2017a). By appropriately selecting the fracture toughness of the pristine host material Γ_0, Li embrittlement effect can be well described by Eq. (45).

2.5. Implementation in finite element modeling

We implement the coupled diffusion-deformation-fracture theory described in Sections 2.1–2.4 into numerical modeling in the finite element software COMSOL Multiphysics™ (COMSOL Multiphysics 5.3, Sweden). The built-in time-dependent solver MUMPS (MUltifrontal Massively Parallel sparse direct Solver) is used to solve the weak formulations of kinematics of deformation in Eq. (17) and kinetics of Li diffusion in Eq. (31). Segregated approach is adopted to improve the convergence. The test functions $\mathbf{v}(\mathbf{X}, t)$ and $\hat{\mu}(\mathbf{X}, t)$ are selected as quadratic Lagrange and linear Lagrange, respectively, to save the computational cost and retain the numerical accuracy at the same time. The co-evolution of Li concentration and stresses are calculated from the field variables $\mathbf{u}(\mathbf{X}, t)$ and $\mu(\mathbf{X}, t)$ via the approaches described in Sections 2.1 and 2.2.

The modified J-integral in Eq. (34) is used to evaluate the driving force (energy release rate) of crack growth in the chemomechanical system. The values of modified J-integral are calculated from four rectangular contours enclosing the crack tip. The path-independence of the modified J-integral is verified by checking the convergence of the values of the modified J-integral from the four independent contours. The mesh around the crack tip is refined to obtain accurate results without the mesh sensitivity. Apart from the Griffith-based LEFM analysis on the onset of crack propagation, an independent numerical calculation is conducted to investigate the dynamic corrosive fracture behavior via the CZM described in Section 2.3. We assume the preexisting crack propagates along its predefined crack plane. Cohesive elements are preset in front of the initial crack along its cracking plane and used to simulate the crack initiation and propagation, as shown in Fig. 2(b). The size of the cohesive elements is much smaller than the characteristic size of the initial crack. The numerical sensitivity on the size of cohesive elements is verified.

3. Results and discussion

3.1. Corrosive fracture in Li insertion and extraction

We study the corrosive fracture of electrodes under concurrent chemical and mechanical load for two successive cracking behaviors – crack initiation and following propagation. We first examine the competitive energy release rate and fracture resistance upon lithiation (delithiation) to predict the onset of crack. Then we model the dynamic stress evolution and Li diffusion coupled with crack propagation after crack initiates. We use a model system of a simplified plane-strain condition embedded with a pre-existing crack, Fig. 2(a), where A and L are the length and thickness of the model, respectively. The crack with a length of a is modeled as a notch with a small but finite tip radius of $\rho \ll a$. The system is subject to both mechanical and chemical load. Mechanical load is set as a constant strain boundary condition ε_0 to mimic the electrodes experiencing a lithiation (delithiation) induced mismatch strain brought by the phase boundaries, constrained grain boundaries, or the mismatch between the active redox material with the conductive matrix and current collectors. Chemical load is set as a constant Li concentration C_0 at the left surface of the model as well as at the crack surface, Fig. 2(a). We assume the mechanical load, stress evolution, and crack growth are much faster than Li diffusion such that the system remains in mechanical equilibrium state while the chemical equilibrium is determined by Li transport.

We will discuss the results of Li insertion and extraction in separate sub-sections. In Section 3.1.1, we focus on the corrosive fracture due to lithiation. The chemical boundary condition drives Li insertion and the lithiated product exhibits a lower fracture resistance as quantitively determined in Eq. (45). In Section 3.1.2, we examine the corrosive fracture upon delithiation. We adopt the description of delithiation embrittlement in Eq. (45) to represent the loss of fracture resistance when Li extracts. We use the material properties for graphite active material in the two sections (Christensen and Newman, 2006; Lin et al., 2013). We set the Young's modulus $E = 15$ GPa, Poisson's ratio $\upsilon = 0.3$, Li diffusivity $D = 3.9 \times 10^{-14}$ m^2/s, partial molar volume of Li in graphite $\Omega = 3.65 \times 10^{-6}$ m^3/mol, and maximum Li concentration $C_{\max} = 26,580$ mol/m^3. To focus on the fracture behavior, we assume that the elastic modulus and Li diffusivity do not vary with the Li concentration. The study on the variation of the elastic modulus can be found in earlier papers (Gao and Zhou, 2013; Sarkar et al., 2017). Here we will use the same set of material properties except the difference in the fracture toughness in lithiation and delithiation – apparently one material cannot experience embrittlement in both Li insertion and extraction. To make the analysis be general, we will use a group of dimensionless parameters to avoid the dependence of results on the specific choice of material properties. The dimensionless parameters are identified as follows: Li concertation $C/C_{\max}$, diffusion time Dt/A^2, stress $\sigma/E\varepsilon_0$, energy release rate $G/E\varepsilon_0^2 L$, fracture toughness $\Gamma/E\varepsilon_0^2 L$, crack length a/A, and the embrittlement effect Γ/Γ_0. Γ/Γ_0 is set to follow Eq. (45) with an exponent $n = 2$. We will also discuss the effect of the embrittlement exponent (i.e. $n = 1$, 2 and 3) in the numerical results.

3.1.1. Li insertion induced material embrittlement and corrosive fracture

The model system contains a pre-existing crack and is subject to the concurrent mechanical and chemical load as described earlier. The mechanical load is prescribed by a remote strain field $\varepsilon_0 = 2\Delta L/L = 0.04$ where ΔL is the displacement applied at the upper and lower surfaces. During lithiation, we set the remote tensile strain always larger than the lithiation-induced linear strain (i.e. $\varepsilon_{Li} = 1/3\log(1 + \Omega C)$) so that the crack closing will not occur. The mechanical boundary condition generates a field of tensile stresses which reduce the chemical potential of Li (Eq. (29)) and promotes Li insertion into the host material. By solving the coupled stress-diffusion equations, Fig. 3(a) plots the distribution of Li concentration along the x-direction ahead of the crack at different lithiation times. The system is initially Li-free (i.e. initial Li concertation $C_i = 0$). Lithiation starts upon applying the chemical load $C_0/C_{\max} = 0.5$, and is terminated when the system reaches the chemical equilibrium. As shown in Fig. 3(a), the surface regime is quickly saturated with Li because of the short diffusion length and the inner region is continually lithiated as the normalized diffusion time Dt/A^2 increases. Li concentration along the diffusive direction (x-direction) does not show a typical distribution of smooth gradient. Instead, a high concentration field of Li exists ahead of the crack tip and the concentration of the singular Li field is much higher than the overall Li concentration within the system. Fig. 3(b) shows Li accumulation ahead of the crack tip and the contour plot of tensile stress at $Dt/A^2 = 0.03$ and $Dt/A^2 = 1.5$, respectively. The inhomogeneous distribution of Li originates from the modulation of the stress field on Li diffusion. Since Li insertion is initiated after applying a tensile load to the system, the mechanical load reduces Li chemical potential and drives Li insertion. The stress concentration ahead of the crack tip absorbs Li toward the crack region. The extra Li driven by the stress field appends a volumetric dilation at the crack tip which reduces the driving force for crack growth. As lithiation proceeds, Li concentration within the system continually increases while the tensile stress field diminishes, as shown in the stress profiles in Fig. 3(b). Li insertion-induced volumetric expansion counterbalances the tensile strain supplied by the external mechanical load, and thus, the overall tensile stresses are reduced. As expected, a higher Li concentration boundary condition contributes to a lower tensile stress field and consequently a lower driving force for crack growth. This stress relaxation behavior is revealed when a larger chemical load C_0 is applied. Fig. 3(c) presents the contour profiles of Li concentration and tensile stresses near the crack tip under different chemical boundary conditions $C_0/C_{\max} = 0.25$, 0.5, 0.75 and 0.9, respectively. When C_0 increases, more Li atoms are pumped into the system which eliminates the average tensile stress in the system as well as the stress singularity near the crack tip.

Upon the decrease of the stress field during lithiation, the driving force of crack growth (i.e. energy release rate G) is reduced. We denote the energy release rate due to pure external mechanical load as G_0. According to LEFM, G_0 is calcu-

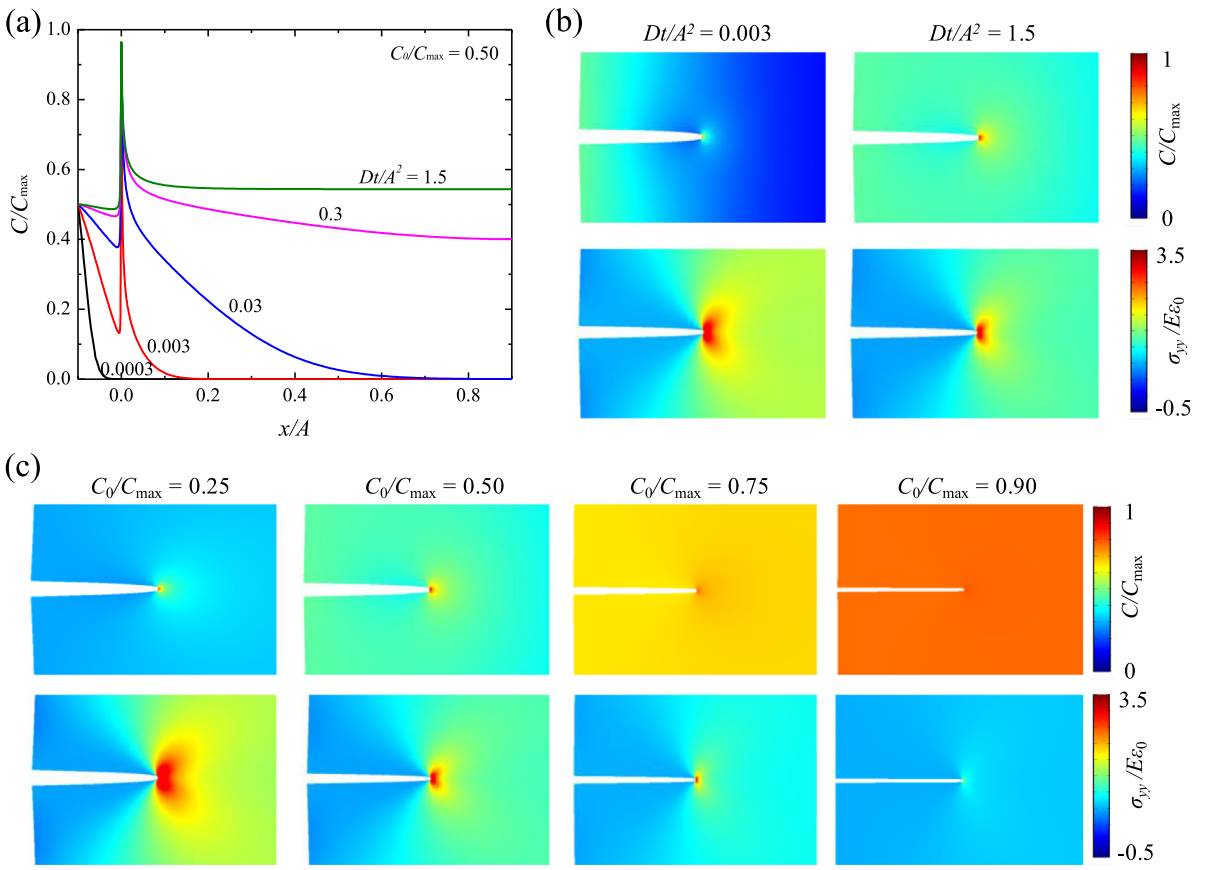

Fig. 3. (a) Li concentration along the crack path in the x-direction with the chemical boundary condition $C_0/C_{max} = 0.5$. (b) The contour profiles of Li concentration and tensile stress near the crack tip at the dimensionless times $Dt/A^2 = 0.003$ and 1.5. (c) The contour profiles of Li concentration and tensile stress near the crack tip under various chemical load $C_0/C_{max} = 0.25$, 0.5, 0.75 and 0.9. The contour profiles are plotted at the time when lithiation is terminated.

lated as $G_0/E\varepsilon_0{}^2L = 0.52$. The energy release rate G for the crack under both mechanical and chemical load can be expressed as $G = G_0 + \Delta G$, where ΔG is the change of the energy release rate induced by the lithiation reaction. Since Li insertion reduces the tensile stress field, ΔG is a negative quantity which is determined by two factors: (i) The extra amount of Li accumulated around the crack tip, and (ii) the volumetric dilation which counterbalances the applied far-field tensile strain. Fig. 4 plots the energy release rate $G = G_0 + \Delta G$ (black lines) as a function of the lithiation time. Two types of chemical load conditions are calculated: $C_0/C_{max} = 0.02$ in Fig. 4(a) and $C_0/C_{max} = 0.20$ in Fig. 4(b). As expected, G gradually decreases upon lithiation from the initial value G_0 and reaches a minimum value when lithiation is completed. In Griffith criterion, the onset of crack growth depends on the relative values of the energy release rate and the material fracture toughness. By assuming a constant fracture toughness of the lithiated phase, a crack during lithiation will be less likely to propagate. Nevertheless, the fracture behavior is more complicated when we consider both the stress-diffusion coupling and Li embrittlement effect. The stress singularity at the crack tip makes the local Li concentration near the crack tip much higher than the concentration boundary condition prescribed by C_0, as is evident in the evolution of Li concentration at the crack tip (blue line) in Fig. 4. Unlike the stress singularity, Li accumulation around the crack tip will not be eliminated when lithiation proceeds. Fig. 4(a) and (b) show that Li concentration near the tip monotonically increases with the lithiation time Dt/A^2. Two factors account for the holding of high Li concentration at the crack tip during the lithiation. First, an early paper proved that (Yang et al., 2011) when a material with a pre-existing crack is subject to both mechanical and chemical load, Li concentration has a $e^{r^{-\frac{1}{2}}}$ singularity around the crack tip which is much higher than the stress singularity $r^{-\frac{1}{2}}$. Therefore, a high Li concentration will be maintained despite the reduction of the stress singularity at the crack tip. Second, although the continuous lithiation eliminates the stress singularity which subsequently reduces the stress-regulated Li accumulation, the overall Li concentration within the host still increases which yields a monotonic increase of Li concentration at the crack tip. As a result, if the Li embrittlement described in Eq. (45) holds, the fracture toughness of the host material continuously decreases as lithiation proceeds. Fig. 4 shows the evolutions of the fracture toughness (red lines) as a function of the lithiation time, in which the initial fracture toughness of the pristine material is set as $\Gamma_0/E\varepsilon_0^2L = 0.8$ and the Li concentration-dependent fracture

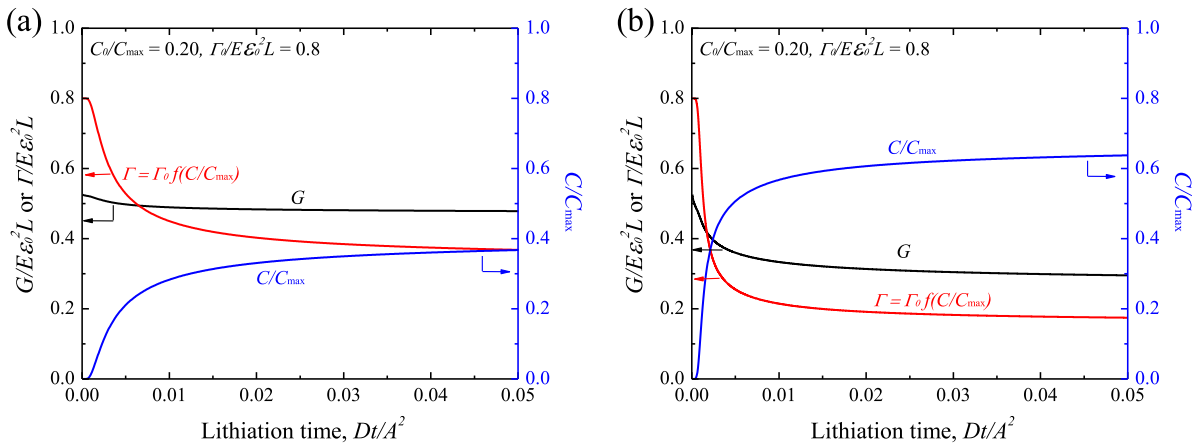

Fig. 4. The evolving Li concentration C/C_{max} at the crack tip (blue line), energy release rate $G/E\varepsilon_0^2 L$(black line), and fracture toughness $\Gamma = \Gamma_0 f(C/C_{max})$ (red line) during lithiation under two chemical load conditions, (a) $C_0/C_{max} = 0.02$, and (b) $C_0/C_{max} = 0.20$. (For interpretation of the references to color in this figure legend, the reader is referred to the web version of this article.)

toughness $\Gamma/E\varepsilon_0^2 L$ is calculated from Eq. (45) by choosing the Li embrittlement exponent $n = 2$. Fig. 4 demonstrates that, although both the energy release rate G and fracture toughness Γ drop upon lithiation, the decrease rate in fracture toughness is larger than that for the energy release rate because of the higher singularity of Li concentration at crack tip. This comparison indicates that crack propagation during lithiation will be triggered more easily, which is a contrary conclusion in the case where the fracture toughness is assumed to be a constant.

In the following discussion, we define the critical time for the onset of crack growth as the time when the energy release rate G equals the fracture toughness Γ, that is $\tau_c = (Dt/A^2)_{G=\Gamma}$. As shown in Fig. 4(a), for chemical load condition $C_0/C_{max} = 0.02$, τ_c is about 0.006 if the host material has a pristine fracture toughness $\Gamma_0/E\varepsilon_0^2 L = 0.8$. τ_c will be larger for the host material of a higher pristine fracture toughness Γ_0, and vice versa. In Fig. 4, a higher value Γ_0 shifts up the red curve and results in a larger value of time for the energy release rate curve intersects with the fracture toughness. Certainly, for a material of sufficiently large Γ_0, fracture toughness Γ can be always higher than the energy release rate G and crack growth is suppressed upon the entire lithiation. In general, the fracture toughness of the host material Γ_0 and its evolution law $\Gamma = \Gamma_0 f(C/C_{max})$ provides the threshold of crack growth and determines the overall crack behavior. Comparing Fig. 4(a) and (b), we also notice that the critical time for crack growth τ_c is dependent on the chemical boundary condition C_0/C_{max}. Specifically, τ_c for the crack under chemical load $C_0/C_{max} = 0.02$ is around 0.006, while τ_c for $C_0/C_{max} = 0.25$ is around 0.002. Although a larger chemical load tends to eliminate the tensile stress field and thus decrease the energy release rate for crack growth, the fracture toughness drops at a much faster rate because of the higher-order singularity of Li concentration at the crack tip as shown in Fig. 4(b). In the limiting case that the chemical load is zero, the energy release rate G is constant ($G/E\varepsilon_0^2 L = 0.52$) and the fracture resistance of the host material remains the initial value ($\Gamma/E\varepsilon_0^2 L = 0.8$), there will be no intersection of the energy release rate with the fracture toughness; thus, the onset time of crack growth is infinity. Overall, the results in Fig. 4 demonstrate that the fracture toughness of pristine host material Γ_0, the Li embrittlement function $\Gamma = \Gamma_0 f(C/C_{max})$, and the chemical load condition C_0/C_{max} all together determine the fracture behavior of the chemomechanical system.

The above analysis based on Griffith fracture mechanics indicates that a crack in a host tends to grow if the material has lower fracture toughness and is subject to a larger chemical load. Crack growth may exhibit two different behaviors: stable and unstable cracking, depending on how the energy release rate G and fracture toughness Γ evolve with the crack extension a (Anderson, 2017). To understand the stable and unstable crack growth, it is convenient to compare the crack driving force curve (i.e. energy release rate G with respect to the crack extension a) and the resistance curve or R curve (i.e. fracture toughness Γ with respect to the crack extension a). The condition for stable cracking can be expresses as $G = \Gamma$ and $dG/da \le d\Gamma/da$ within a finite crack extension da, while the unstable cracking occurs when $G = \Gamma$ and $dG/da > d\Gamma/da$.

For the system subject to the only mechanical load of a constant far-field strain, the energy release rate $G/E\varepsilon_0^2 L = 0.52$ is nearly independent of crack extension and the fracture toughness also remains as its initial value. Once the energy release rate G exceeds the fracture toughness Γ, crack would propagate unstably because the driving force is always higher than the resistance of crack growth. However, for the chemomechanical system under both mechanical and chemical load, the driving force and the resistance curves both evolve with the crack extension and should be carefully analyzed. Fig. 5(a) plots the normalized energy release rate $G/E\varepsilon_0^2 L$ as a function of crack extension upon lithiation with a chemical load $C_0/C_{max} = 0.5$. According to the Li concentration distribution in Fig. 3(a), the crack extension shifts the crack tip from the Li-rich to the Li-poor region, recovering the high tensile stress around the crack tip and the associated driving force for crack growth. Therefore, energy release rate G increases as crack propagates for the entire lithiation time, Fig. 5(a). We analyze the fracture behavior at a specific time $Dt/A^2 = 0.03$ and assume that the Griffith fracture criterion $G = \Gamma$ is satisfied. The energy release

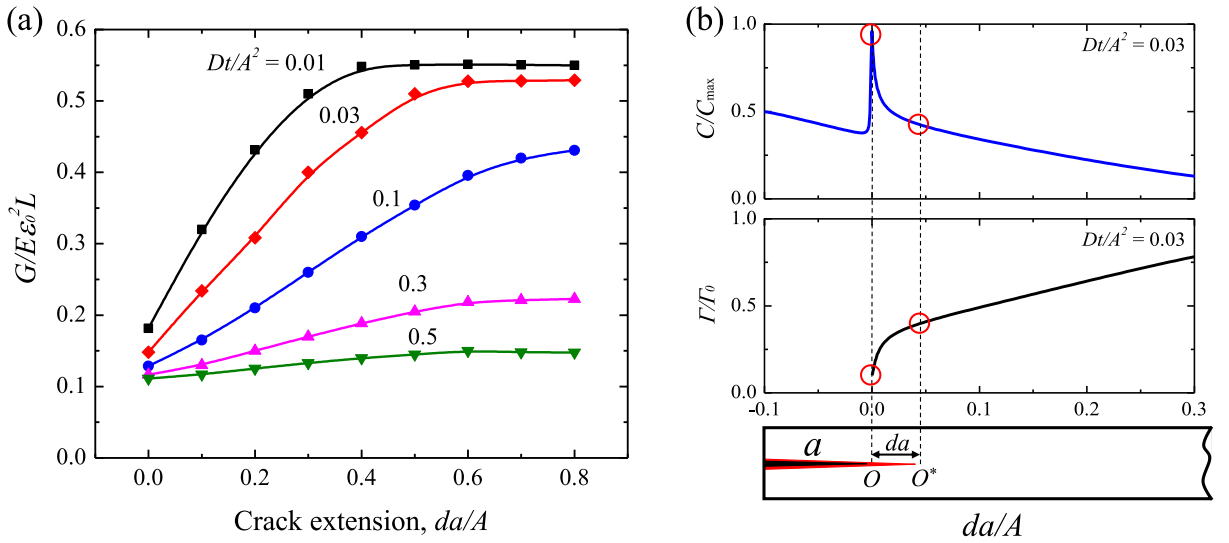

Fig. 5. Plots of crack driving force G and crack resistance Γ. (a) Energy release rate $G/E\varepsilon_0^2 L$ as a function of the normalized crack extension da/A at different lithiation times. G increases as crack extends because the crack tip migrates from the Li-rich zone to the Li-poor regime. (b) Li concentration C/C_{max} (upper figure) and fracture toughness $\Gamma_0/E\varepsilon_0^2 L$ (lower figure) near the crack tip at $Dt/A^2 = 0.03$. When the crack tip propagates from O to O*, fracture toughness Γ of the host material at the fresh crack tip recovers to a larger value and resists further growth of the crack. Crack growth resumes after Li accumulates around the new crack by diffusion.

rate curve at this time $Dt/A^2 = 0.03$ is shown as the red curve in Fig. 5(a). To obtain the resistance curve, we first determine the Li distribution C/C_{max} near the crack tip when the crack propagates a distance of da. The corresponding Li profile is shown in the upper graph of Fig. 5(b). Then, using the Li embrittlement formula in Eq. (45), the fracture toughness $\Gamma/E\varepsilon_0^2 L$ of the host material near the crack tip can be estimated and is shown in the lower graph of Fig. 5(b). The early discussion has demonstrated that crack propagation during lithiation is triggered more easily. Before the crack grows, Li accumulation at the crack tip always exists owing to the tensile stress singularity at crack tip. Once the fracture toughness of host material at the tip drops to be lower than the driving force for crack growth, crack propagates by a characteristic length da. Since the crack propagation is much faster than the Li diffusion, the crack tip would be immediately shifted away from the region of Li accumulation, as shown in the Li profile in Fig. 5(b). Without the Li embrittlement at the Li-concentrated regime, the fracture toughness Γ at the fresh crack tip recovers to a higher level, as shown in the lower panel of Fig. 5(b). By comparing the driving force curve in Fig. 5(a) and the resistance curve in Fig. 5(b), the conditions for stable cracking $G = \Gamma$ and $dG/da \leq d\Gamma/da$ are indeed met. Therefore, the crack will propagate by a small distance, and then is arrested until the fracture strength of the host material at the fresh crack tip is weakened again by the following Li redistribution. In this case, the corrosive fracture behaves as a typical delayed fracture of the feature of the "wait and go" behavior – the "wait" depends on the Li transport and the supply of Li at the crack tip, and the "go" depends on the Li embrittlement of the host (Huang et al., 2013; Xu and Zhao, 2016a).

The delayed fracture is a dynamic process that does not only include the crack initiation upon lithiation but also involves the co-evolution of stress field and Li diffusion after the crack grows. To capture the dynamic, we use the CZM method to simulate the dynamic crack propagation as well as the stress and diffusion fields. The crack starts propagation once the energy release rate exceeds the Li concentration-dependent fracture toughness of the cohesive elements which are preset along the cracking plane. The time scale for crack growth and stress generation is much faster than that for Li redistribution, thus, the system is in a chemical transition state unless lithiation is completed or the crack penetrates through the system.

As discussed above, the pristine fracture toughness of the host material Γ_0 and the chemical load C_0/C_{max} are the key parameters determining the fracture behavior. Here we identify different fracture behaviors on a plane spanned by C_0/C_{max} (the chemical boundary condition) and $\Gamma_0/E\varepsilon_0^2 L$ (the normalized pristine fracture toughness). In Fig. 6(a), each point in the plane represents one complete simulation with a given set of values of C_0/C_{max} and $\Gamma_0/E\varepsilon_0^2 L$. The phase diagram in Fig. 6(a) delineates three types of fracture behaviors: the unstable, arrested, and delayed fracture zones. For the chemomechanical system composed of a host of a high pristine fracture toughness and is loaded by small Li concentration (i.e. upper left region), the pre-existing crack remains arrested during the entire lithiation process. In this safe regime, the material flaws will not expand due to the high fracture resistance and low chemical load. On the other side, when the pristine fracture toughness is relatively low and a sufficient Li source is supplied (upper right region), crack propagates when the energy release rate exceeds the fracture toughness, then stops and waits for the Li to reaccumulate at the new crack tip, giving the delayed fracture upon lithiation. The boundary between the regions of arrested fracture and delayed fracture are estimated by connecting the neighboring simulation points in-between the two regimes. As expected, the boundary starts from the

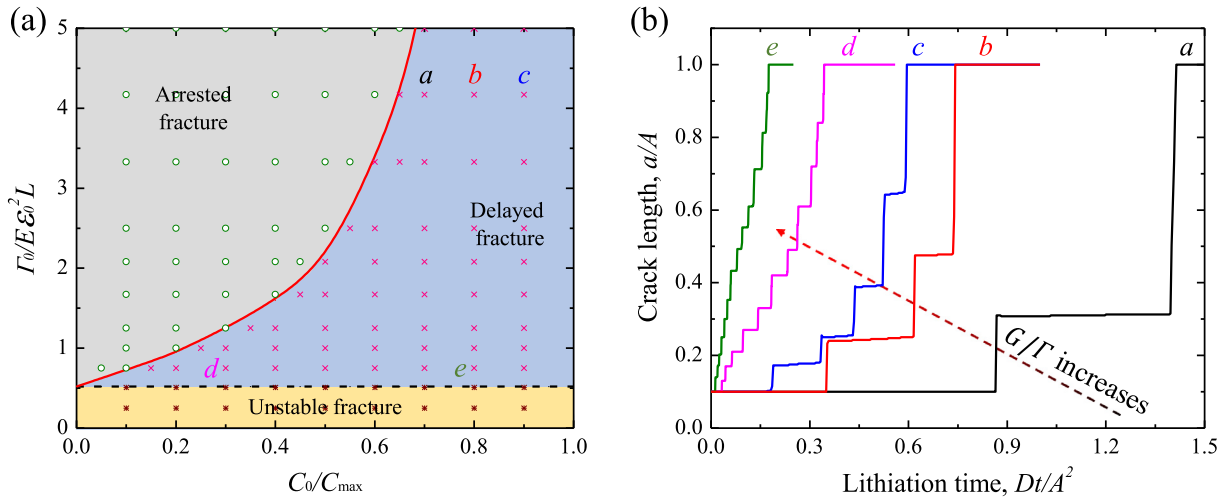

Fig. 6. (a) The phase diagram of corrosive fracture composed of unstable fracture, arrested fracture, and delayed fracture on the plane spanned by the fracture toughness of the pristine host material $\Gamma_0/E\varepsilon_0^2L$ and the chemical load C_0/C_{max}. Each single point in the diagram represents one complete simulation with given values of C_0/C_{max} and $\Gamma_0/E\varepsilon_0^2L$. Boundaries delineating different regimes are estimated by connecting the neighboring points. (b) The evolution of crack length as a function of the lithiation time for various combinations of $\Gamma_0/E\varepsilon_0^2L$ and C_0/C_{max} in the delayed fracture zone. Different lines correspond to the points *a*–*e* in (a). The ratio of the energy release rate to the fracture toughness increases from *a* to *e* which induces the transition from the "wait-and-go" behavior to the unstable fracture.

material toughness $\Gamma_0/E\varepsilon_0^2L = 0.52$ and the chemical condition $C_0/C_{max} = 0$ where the fracture toughness is identical to the energy release rate $G_0/E\varepsilon_0{}^2L = 0.52$ applied by the external mechanical load as discussed in the Fig. 4. If the pristine fracture toughness is below this critical value, no matter whether the system is subject to the chemical load, the energy release rate G_0 induced by the far-field mechanical load already exceeds the fracture resistance and causes unstable cracking, as shown by the regime with the dashed line boundary $\Gamma_0/E\varepsilon_0^2L = 0.52$.

Among the three types of fracture behaviors, the delayed fracture that involves the co-evolution of stress field and Li transport is of particular interest. Fig. 6(b) plots the evolution of the crack length as a function of the lithiation time for different sets of $\Gamma_0/E\varepsilon_0^2L$ and C_0/C_{max}, marked as the points *a, b, c, d*, and *e* in the delayed fracture zone in the phase diagram. In the comparison from *a* to *c* of the same fracture resistance, the time of "wait" depends on the supply of Li and a smaller chemical load allows for a longer time for crack to wait until the next jump in crack length. Overall, the ratio of the energy release rate to the fracture toughness increases from point *a* to point *e* that induces a transition from the "wait and go" delayed crack to the unstable cracking behavior. Fig. 7(a) shows the details of the crack evolution as a function of lithiation time for $C_0/C_{max} = 0.8$ and $\Gamma_0/E\varepsilon_0{}^2L = 4.2$ (point *b* in the phase diagram). The crack propagates by a "go and wait" behavior in which the crack "goes" at the transition of I–II, III–IV, and V–VI, and "waits" at II–III and IV–V. The "go" state represents the rapid crack propagation such that the crack length versus lithiation time exhibits a pulsed jump in Fig. 7(a). The slow redistribution of Li cannot catch the fast crack propagation, resulting in the recovery of fracture toughness at the fresh crack tip and the temporary arrest of the crack growth. The corresponding Li concentration profiles before and after the "go" state are shown in Fig. 7(b). Followed each rapid growth of crack is the "wait" state during which the crack is arrested and the crack length remains a constant. As shown in Fig. 7(b), Li gradually accumulates at the crack tip in the "wait" state until the fracture toughness drops below the energy release rate again. Fig. 7(c)–(e) shows the schematics of delayed fracture due to the concurrent Li diffusion, Li embrittlement, and crack growth. While the crack "waits", the crack remains a steady state. Li accumulates around the crack tip due to the stress concentration which weakens the fracture strength of the host material. When the fracture resistance is below the energy release rate, crack propagates and creates fresh surfaces without Li. Without the Li embrittlement effect, the fracture resistance increases and crack stops. The "go" and "wait" repeat while Li diffuses and crack grows.

In the phase diagram of corrosive fracture, we have demonstrated that the fracture toughness and the chemical load play the major role in regulating the fracture behavior of the chemomechanical system. The two factors both originate from the stress modulated Li diffusion and Li-assisted embrittlement. Next, we would like to explore in detail the effect of stress-diffusion coupling and Li embrittlement by evaluating each factor separately. We first examine the sensitivity of the degree of Li embrittlement on the phase diagram. As written in Eq. (45), the degree of embrittlement is represented by the exponent *n* where a larger value of *n* indicates severer embrittlement due to Li insertion. Fig. 8(a) shows the fracture toughness of the host material as a function of the Li concentration for three different embrittlement exponents $n = 1$, 2, and, 3. It is clear that the fracture toughness of the host material reduces as Li inserts and a higher exponent *n* induces more degradation of the fracture strength except the setting values at the initial and the final Li concentrations. Using the same procedure in Fig. 6(a), we construct the phase diagrams of the three different embrittlement exponents in Fig. 8(b).

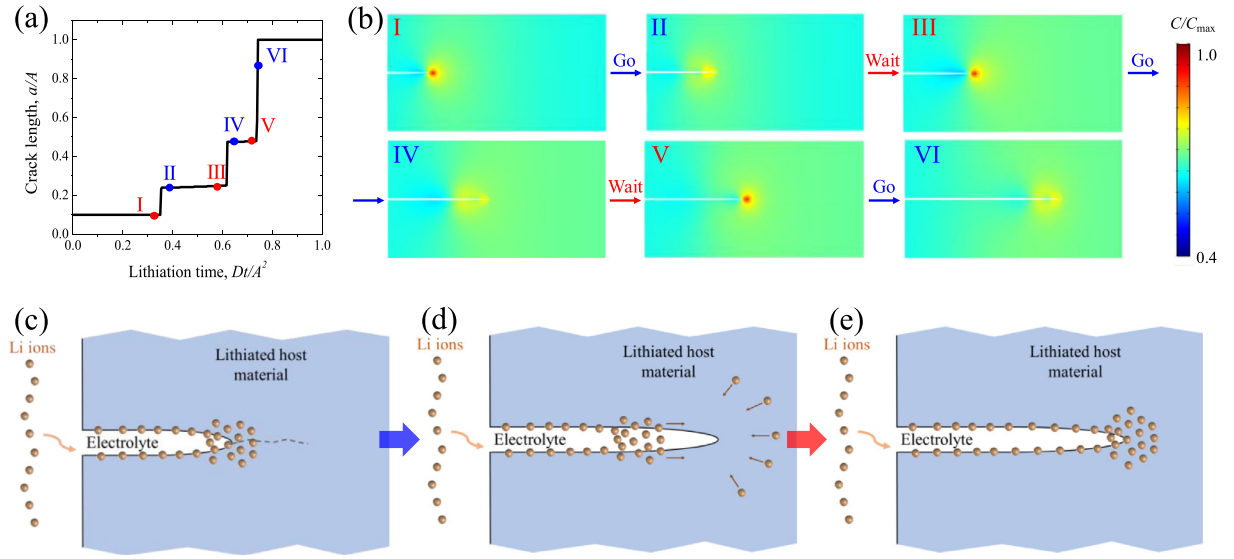

Fig. 7. (a) The plot of crack length upon lithiation for $C_0/C_{max}=0.8$ and $\Gamma_0/E\varepsilon_0^2L=4.2$ (point *b* in Fig. 6(a)). The crack propagation is a typical "wait-and-go" behavior in which the crack "goes" at the transition of I–II, III–IV, and V–VI, and "waits" at II–III and IV–V. (b) The corresponding profiles of Li concentration at the lithiation times I–VI. (c)–(e) Schematics of delayed fracture due to the concurrent Li diffusion, Li embrittlement, and crack growth. (c) While the crack "waits", the crack remains in a steady state. Li accumulates around the crack tip due to the stress concentration and weakens the fracture strength of the host material. (d) When the fracture resistance is below the energy release rate, crack propagates and creates fresh surfaces without Li. Without the Li embrittlement effect, the fracture resistance increases and crack stops. (e) The "go" and "wait" repeat while Li diffuses and crack grows.

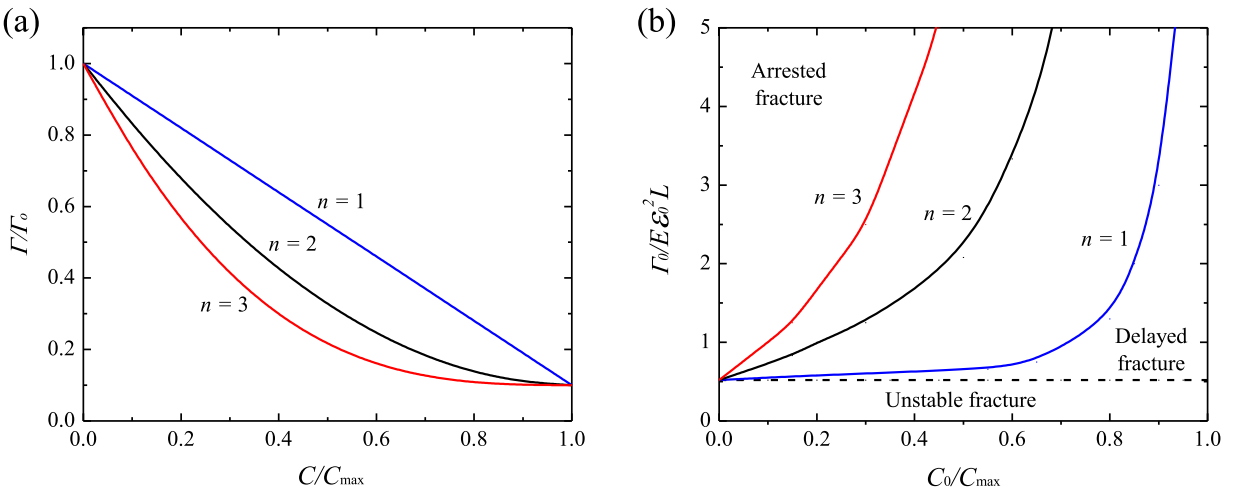

Fig. 8. (a) Fracture toughness of the host material as a function of the Li concentration for different embrittlement exponents $n=1$, 2, and 3. A larger value of n represents a severer Li embrittlement effect. (b) Phase diagram of corrosive fracture with a variation of the embrittlement exponent. When the embrittlement exponent increases, the size of the arrested fracture zone is reduced while the region of delayed fracture is enlarged.

With a different set of embrittlement function, the border lines separating the different fracture zones are largely shifted. Comparing to the phase diagram for $n=2$, a severer Li embrittlement ($n=3$) reduces the size of the arrested fracture regime (safe region) and the delayed fracture occupies most space of the variable plane. In this case, the chemomechanical system becomes more sensitive to the material defects and flaws and the mechanical integrity is vulnerable upon lithiation. On the other side, when the Li embrittlement is less severe ($n=1$), the region of arrested fracture is enlarged and the pre-existing flaws is less likely to propagate during the Li reaction.

Next, we examine the influence from the stress-regulated Li diffusion on the corrosive fracture behavior. We rewrite Eq. (29) by introducing a non-dimensional parameter χ that represents the degree of the stress effect on Li diffusion,

$$\mu=\mu_0+kT\ln\left(\frac{C}{C_{max}-C}\right)-\chi\Omega\sigma_m. \tag{46}$$

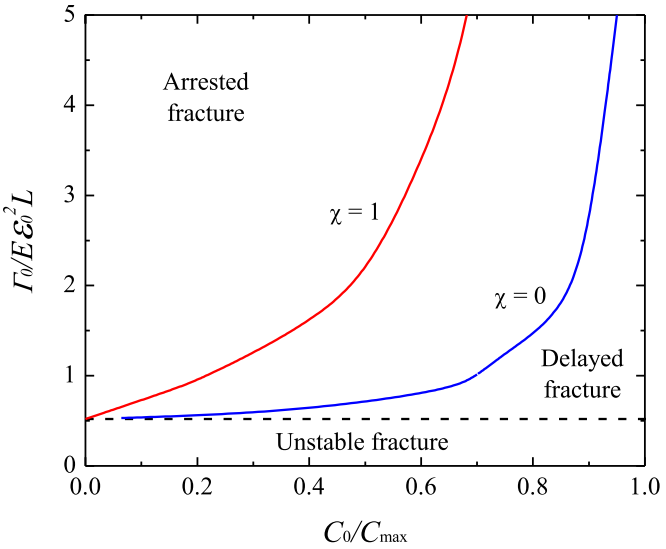

Fig. 9. Comparison of the phase diagrams with ($\chi = 1$) and without ($\chi = 0$) considering the stress effect on Li diffusion. By considering the stress-diffusion coupling ($\chi = 1$), the stress field near the crack tip regulates Li accumulation and promotes embrittlement. Therefore, the arrested fracture zone (safe region) shrinks in size and the delayed fracture zone increases on the variable space.

Specifically, χ can be varied from 0 to 1 in which $\chi = 1$ includes the stress effect on Li diffusion for the isotropic-expansion host during Li insertion, and $\chi = 0$ ignores the stress-diffusion coupling. Fig. 9 plots the comparison of the phase diagrams with ($\chi = 1$) and without ($\chi = 0$) considering the stress effect on Li diffusion. When the stress effect is accounted ($\chi = 1$), the high tensile stress near the crack tip promotes Li embrittlement by regulating the Li accumulation near the crack tip. As a result, the region of the arrested fracture (safe region) shrinks in size and the delayed fracture is more dominant on the variable space. We may consider that the stress-diffusion coupling acts like a catalyst which accelerates the Li transport and expediates the corrosive fracture of the host material. Conversely, in the hypothetical scenario that Li is only supplied by the chemical boundary condition and is not influenced by the local stress field ($\chi = 0$), the delayed fracture is much less likely to occur.

3.1.2. Li extraction induced material embrittlement and corrosive fracture

The delithiation-induced fracture in electrodes has been extensively studied (Woodford et al., 2010; Zhao et al., 2010; Ryu et al., 2011). Li extraction is usually accompanied with a volumetric contraction of electrodes which induces a field of tensile stress and causes crack formation. To examine the corrosive fracture during the delithiation process, we assume that the host is initially at the fully lithiated state (i.e. initial Li concertation $C_i = C_{max}$). Delithiation starts upon applying the chemical load $C_0/C_{max} = 0.5$, and is terminated when the system reaches chemical equilibrium. During delithiation, the system is free of the external mechanical load ($\varepsilon = 0$) so that the stress field is solely due to the delithiation induced volumetric contraction. This type of chemomechanical boundary condition was widely used to simulate the delithiation of spherical active particles or thin film electrodes constrained by a substrate (Gao and Zhou, 2013).

Fig. 10(a) shows the distribution of Li concentration along the crack path in the x-direction in the course of delithiation. Li close to the surface is quickly depleted while the Li concentration in the inner regime remains high. The mismatch strain generates a field of tensile stress in the Li-poor regime near the surface and compressive stresses in the Li-rich regime. Once delithiation proceeds toward the inner regime, a stress singularity at the crack tip emerges which attracts Li accumulation at the crack zone, Fig. 10(a). Even though the average Li concentration in the system decreases during delithiation, Li concentration near the crack tip remains a large value as seen in Fig. 10(a) and (b). Li retention at crack tip is attributed to the tensile stress in the host, especially near the crack tip, which continuously increases upon delithiation that traps Li via the stress regulated Li distribution.

In addition to modulating Li accumulation around the crack tip, the growing stress singularity upon delithiation also increases the driving force for crack growth. Fig. 10(c) plots the energy release rate $G/E\varepsilon_0{}^2L$ (black line) as a function of the delithiation time with a chemical load $C_0/C_{max} = 0.5$. Energy release rate starts from zero (i.e. $G_0 = 0$) since no mechanical force is applied, and monotonously increases as delithiation proceeds. The fracture toughness (red line) at the crack tip is determined by the local Li concentration (blue line), Fig. 10(c). Li retention at the crack tip remains higher than 80% of C_{max} during the entire delithiation. Considering the delithiation-induced embrittlement described in Eq. (45), the average fracture toughness of the system significantly drops as Li depletes, however, the fracture toughness near the crack tip remains a high value because the Li accumulation at the crack tip which prevents the host from the embrittlement effect. As the energy release rate G increases and the fracture toughness of the delithiated phase reduces, delithiation generally promotes crack

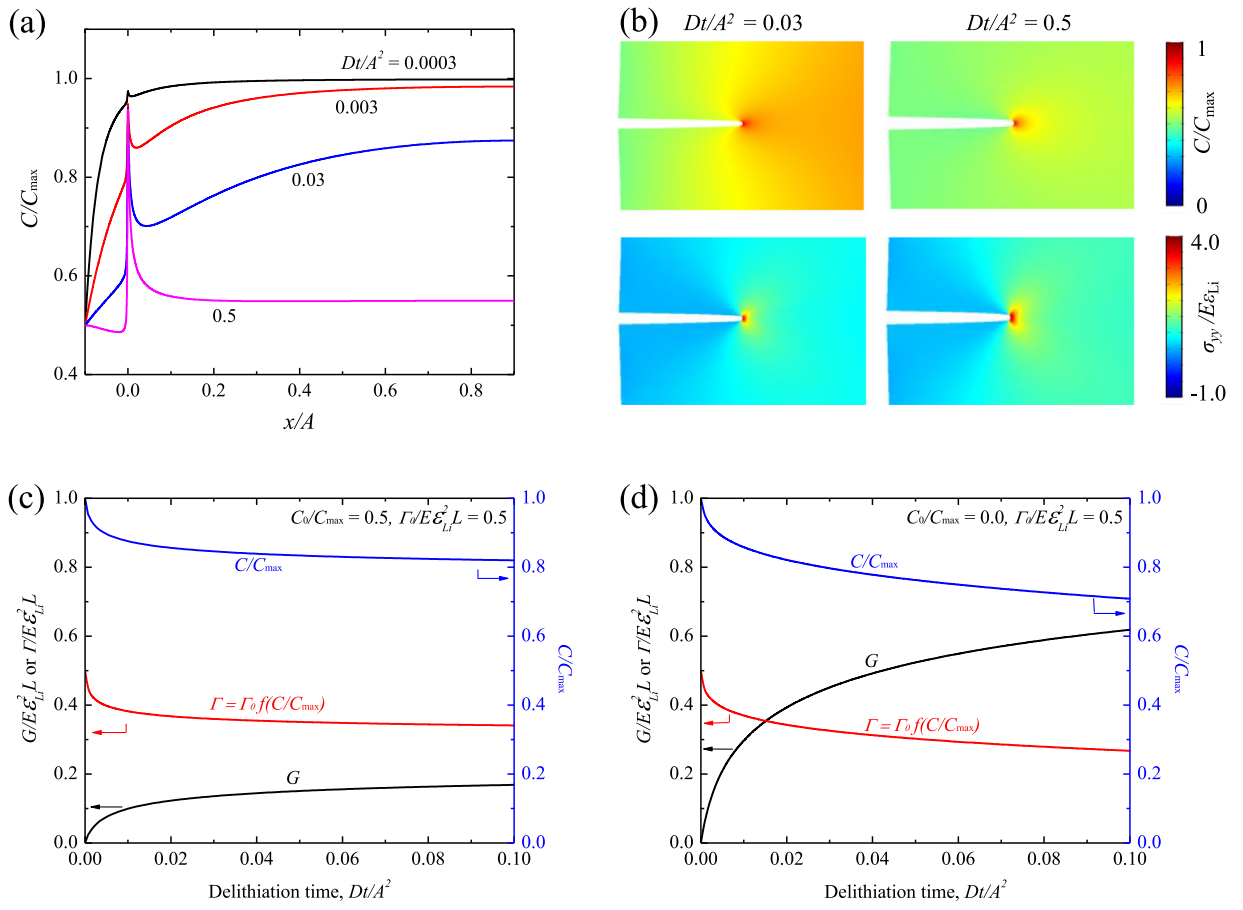

Fig. 10. (a) The distribution of Li concentration along the crack path in the *x*-direction during delithiation with the chemical boundary condition $C_0/C_{max} = 0.5$. (b) The contour profiles of Li concentration and tensile stress near the crack tip at $Dt/A^2 = 0.03$ and 0.5. (c), (d) The evolving of Li concentration C/C_{max} at the crack tip (blue line), energy release rate $\Gamma_0/E\varepsilon_{Li}^2 L$ (black line), and fracture toughness $\Gamma = \Gamma_0 f(C/C_{max})$ (red line) for the chemical load $C_0/C_{max} = 0.5$, and (d) $C_0/C_{max} = 0$. (For interpretation of the references to color in this figure legend, the reader is referred to the web version of this article.)

growth. Nevertheless, the shielding effect from the stress regulated Li accumulation may postpone the crack propagation as shown in Fig. 10(c). Similarly, Fig. 10(d) shows the Li concentration (blue line) at the crack tip, energy release rate (black line), and fracture toughness (red line) of the host at the crack tip in terms of the delithiation time for a larger chemical load, $C_0/C_{max} = 0$. A larger chemical load results in a higher energy release rate for crack growth and a lower fracture toughness of the host which causes crack growth during delithiation.

We next examine the growth behavior of the crack once it starts propagating during Li extraction. Fig. 11(a) plots the driving force of crack growth in which the energy release rate $G/E\varepsilon_{Li}{}^2 L$ at various delithiation times Dt/A^2 are plotted as a function of the normalized crack extension da/A. During delithiation, the regime away from the surface is less delithiated such that the magnitude of the tensile stress in the inner regime is smaller. Once the crack growth initiates, crack migrates from the Li-poor regime of high tensile stresses to the inner Li-rich regime of low tensile stresses which reduces the energy release rate, Fig. 11(a). Without considering the Li embrittlement, the fracture toughness of the system would remain constant during Li extraction. In this case, the condition for stable crack growth will be satisfied, i.e. $dG/da < d\Gamma/da$, once the crack starts to propagate. Therefore, the system behaves as a delayed fracture (Klinsmann et al., 2016a). If we consider the fact that the fracture toughness is determined by the Li concentration via the embrittlement effect, we can calculate the fracture toughness (lower graph, Fig. 11(b)) based on the Li concentration distribution near the crack tip (upper graph, Fig. 11(b)). Here we assume the driving force and fracture resistance satisfy the Griffith's criterion $G = \Gamma$ at the time $Dt/A^2 = 0.03$. Once the crack starts to propagate, crack tip immediately migrates away from the Li-accumulated regime. At the fresh crack tip, the material fracture toughness decreases. In this scenario, the growth of crack stops when $dG/da \le d\Gamma/da$ within a finite crack extension da and resumes when the energy release rate overcomes the fracture resistance. This behavior is also a typical "go and wait" delayed fracture.

We perform the cohesive zone modeling to construct the phase diagram of corrosive fracture upon delithiation, Fig. 12. Since there is no external mechanical load, only two types of fracture behaviors are identified: arrested and delayed fracture.

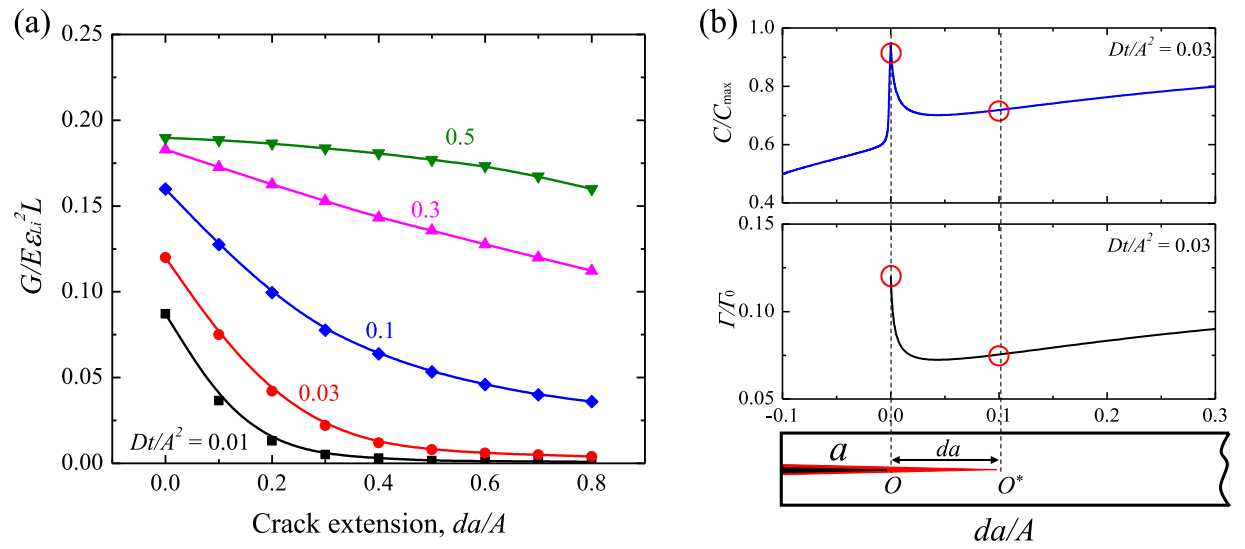

Fig. 11. Energy release rate G and crack resistance Γ during Li extraction. (a) Energy release rate $G/E\varepsilon_{Li}^2 L$ as a function of the normalized crack extension da/A at different delithiation times. G decreases as crack extends because the crack tip migrates from the Li-poor zone to the Li-rich regime. (b) Li concentration C/C_{max} (upper figure) and fracture toughness Γ/Γ_0 (lower figure) near the crack tip at $Dt/A^2 = 0.03$. When the crack tip propagates from O to O*, fracture toughness Γ of the host material at the new crack tip decreases. Crack growth stops when $dG/da \le d\Gamma/da$ and resumes when the energy release rate overcomes the fracture resistance.

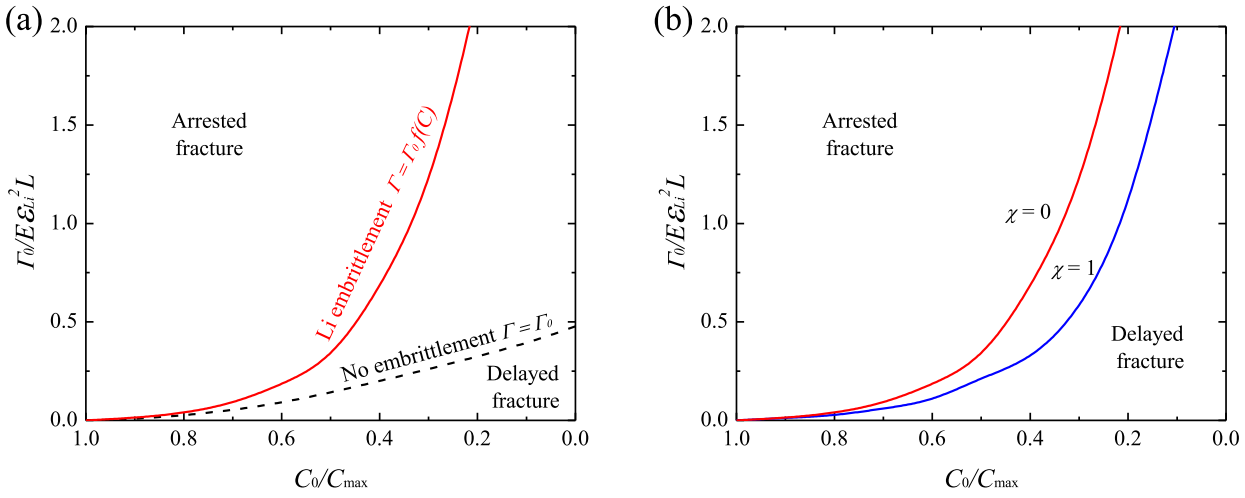

Fig. 12. (a) Comparison of the phase diagrams of corrosive fracture with (red line) and without (black dashed line) considering the Li embrittlement effect. (b) The comparison with ($\chi = 1$) and without ($\chi = 0$) considering the stress-diffusion coupling. (For interpretation of the references to color in this figure legend, the reader is referred to the web version of this article.)

We first examine the effect of the Li embrittlement on the corrosive fracture of the chemomechanical system. The phase diagrams in Fig. 12(a) in terms of C_0/C_{max} and $\Gamma_0/E\varepsilon_0^2 L$ are obtained with and without considering the Li embrittlement effect. C_0/C_{max} are selected from 1 to 0 to represent the degree of delithiation from low to high, respectively. The Li embrittlement enlargers the size of the delayed fracture (lower right zone) which increases the potential of crack propagation upon delithiation. This demonstrates that Li embrittlement makes the chemomechanical system more vulnerable to defects and flaws, and thus deteriorates the mechanical integrity upon delithiation.

We then investigate the effect of stress regulated diffusion on the corrosive fracture during delithiation. Fig. 12(b) plots the phase diagrams with ($\chi = 1$) and without ($\chi = 0$) considering the stress effect on Li diffusion. As discussed in Fig. 9, stress-regulated diffusion upon lithiation acts like a catalyst that promotes Li embrittlement and deteriorates the mechanical integrity of the system. Conversely, the stress-regulated diffusion during delithiation provides a shielding effect on Li embrittlement because the local tensile stress traps Li around the crack tip such that the host material retains a high local Li concentration upon Li extraction. Therefore, when the coupling effect between stress and diffusion is considered ($\chi = 1$), the arrested fracture zone expands in its size while the delayed fracture regime shrinks, Fig. 12(b).

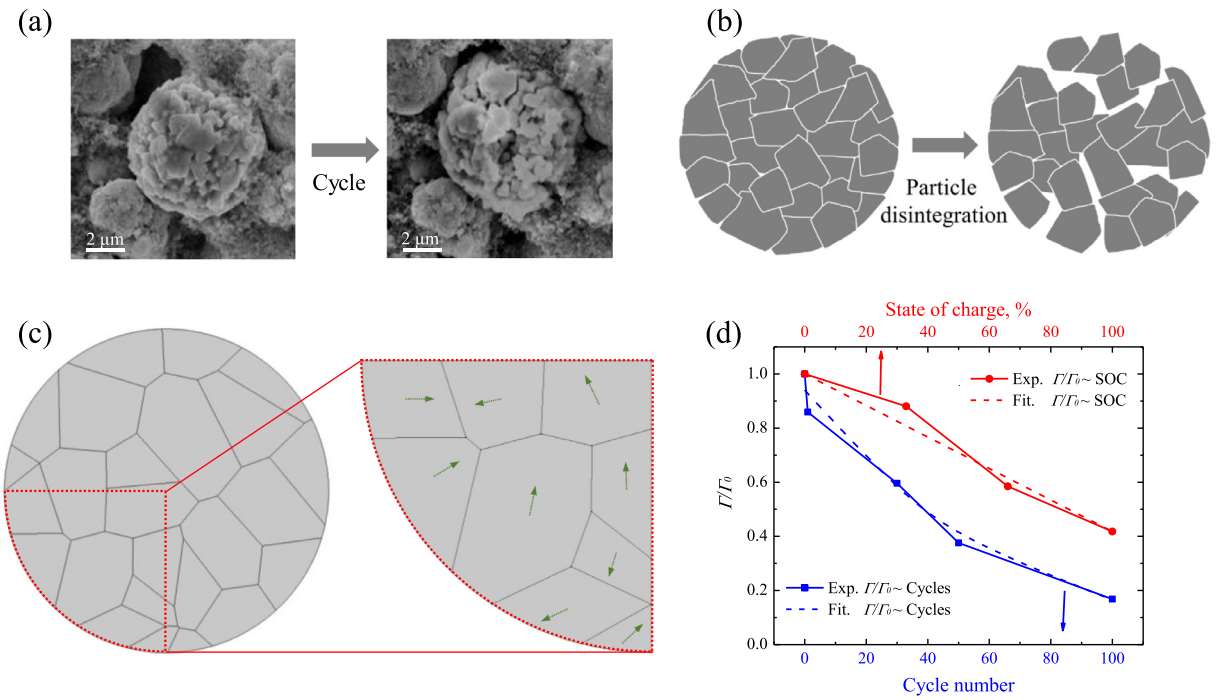

Fig. 13. (a) SEM images and (b) schematics showing heavy intergranular fracture in NMC cathode materials. (c) A model of a spherical NMC secondary particle consisting of irregular primary particles. A quarter of the spherical particle is used in the finite element modeling of intergranular fracture induced by Li reactions. The arrows indicate the *c*-axis orientation within each grain. (d) Fracture strength of NMC is highly dependent on the state of charge and the cycle number. The experimental values are measured by nanoindentation and reproduced from a previous publication (Xu et al., 2017a).

3.2. Corrosive fracture in NMC cathode

We use the theory of corrosive fracture to simulate the intergranular fracture in NMC cathode materials. NMC is the state-of-the-art cathode for the application of electric vehicles, owing to its low cost, excellent cyclic stability, and tunable electrochemical properties (Sun and Zhao, 2017). The synthesis process results in a hierarchical microstructure in NMC where small primary particles of submicron size aggregate via weak interactions and form secondary particles of tens of micrometers (Kim et al., 2016). The cohesion strength of the primary particles is weak, thus the grain boundaries is subject to intergranular cracks generated by the mismatch strains among the primary particles during Li reactions. Specifically, experiments have shown that NMC secondary particles can easily disintegrate into isolated clusters over cycles which mechanically degrades the electrodes and deteriorates the electrochemical performance of batteries. Fig. 13(a) and (b) show the experimental observation and sketch of the structural disintegration of the NMC particles. We used nanoindentation to determine that the interfacial strength of NMC particles is largely dependent on the state of charge and the cycle number (Xu et al., 2017a). The interfacial fracture toughness between primary particles decreases upon delithiation and steadily fades as the electrochemical cycles proceed, presumably because of the accumulation of microscopic defects and damages at the interfaces between the constituent primary particles.

In this section, we model the corrosive behavior of intergranular cracks in an NMC secondary particle upon Li cycles and compare with experiments. We simplify the spherical 3D particles into a more computationally tractable 2D plane-strain model with a radius $R = 5$ μm. The NMC secondary particle is represented by a circular domain composed of multiple primary particles of random sizes and shapes, Fig. 13(c). The polygonal primary particles are generated using the Voronoi tessellation. To reduce the computational cost, a quarter of the spherical particle is used in the finite element modeling. Every primary particle within the model has its own grain orientation and the orientation of *c*-axis is indicated by the arrows in Fig. 13(c). NMC has a layered structure where Li, O, and transition metals occupy alternating atomic layers. The lattice strain associated with Li reactions is highly anisotropic. We use $LiNi_{0.6}Mn_{0.2}Co_{0.2}O_2$ (NMC622) as a model system and simulate the delithiation process from $LiNi_{0.6}Mn_{0.2}Co_{0.2}O_2$ to $Li_{0.5}Ni_{0.6}Mn_{0.2}Co_{0.2}O_2$. We set the strains in the *a*-axis (b-axis) and *c*-axis to be −2% (compressive) and 1% (tensile), respectively, according to the Bragg peak shifting in *in-situ* XRD scanning experiments (Ryu et al., 2018). The magnitude of the anisotropic strain during Li extraction is assumed to be proportional to Li concentration. We implement the experimental results of Li embrittlement on the interfacial fracture toughness into the numerical simulation. The evolving interfacial strength at different states of charge and different cycle numbers is fitted to the experimental values (Xu et al., 2017a), Fig. 13(d). The material properties for NMC622 are selected as follows: Young's modulus $E = 140$ Gpa (Vasconcelos et al., 2016; Xu et al., 2017a), Poisson's ratio $\upsilon = 0.3$, Li diffusivity $D =$

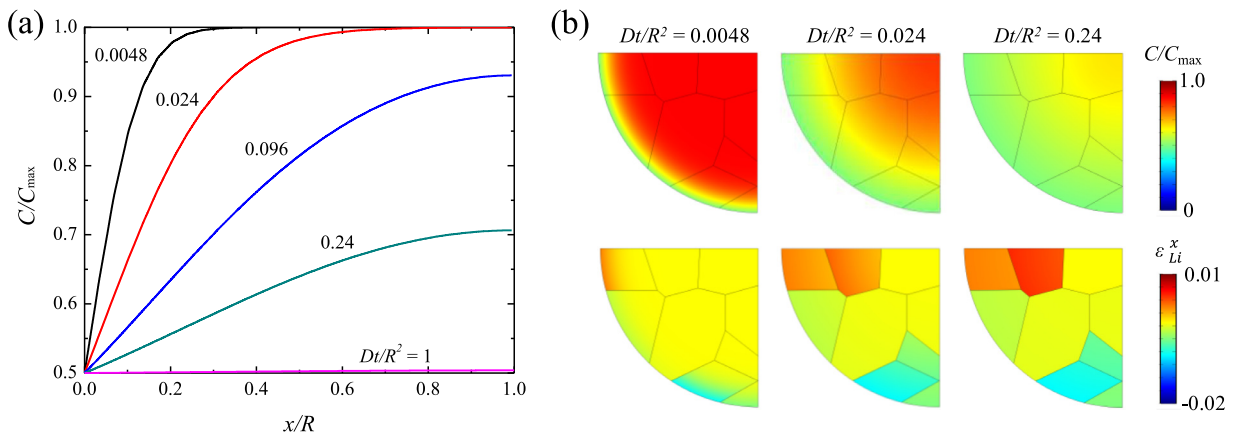

Fig. 14. (a) Radial distribution of Li concentration in the NMC secondary particle under the delithiation load $C_0/C_{max} = 0.5$. (b) The contour profiles of Li concentration and delithiation-induced strain at delithiation times $Dt/R^2 = 0.0048$, 0.024 and 0.24, respectively.

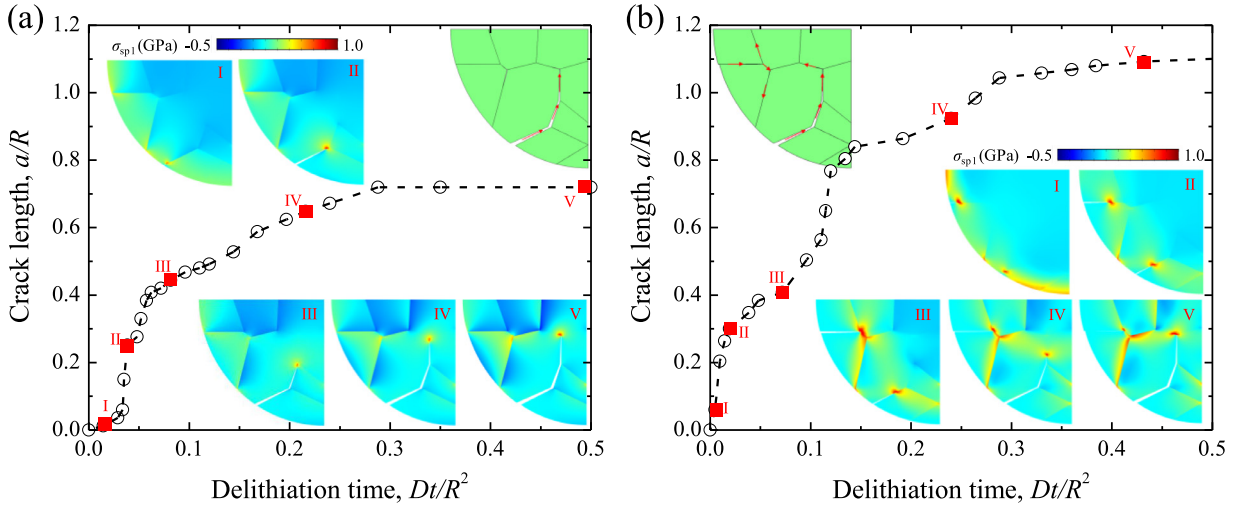

Fig. 15. The evolution of intergranular cracks in NMC cathode during delithiation without (a) and with (b) Li embrittlement effect. Insets show the contour plots of the first principal stress at various delithiation times and their corresponding crack morphologies. The arrows indicate the crack growth paths. For a better view, the deformation of the interfacial cracks has been amplified by a factor of 3.

7×10^{-15} m^2/s (Cui et al., 2016) and $C_{max} = 35,164$ mol/m^3. Several dimensionless quantities are identified: Li concentration C/C_{max}, diffusion time Dt/R^2, fracture toughness $\Gamma/E\varepsilon_{Li}^2 R$, and crack length a/R. ε_{Li} is set as the lattice strain 2% (−2%) along the a-axis upon lithiation (delithiation).

3.2.1. Intergranular cracks in NMC upon delithiation

We first examine the corrosive behavior of intergranular cracks in NMC in the initial delithiation. The NMC particle is at the fully lithiated state ($C_i/C_{max} = 1$) before delithiation starts. A constant chemical load $C_0/C_{max} = 0.5$ is applied on the surface of the NMC aggregated particle to mimic the delithiation process from the initial state $LiNi_{0.6}Mn_{0.2}Co_{0.2}O_2$ to the final product $Li_{0.5}Ni_{0.6}Mn_{0.2}Co_{0.2}O_2$. This chemical boundary condition of Li exchange is analogous to a potentiostatic operation of a battery cell. Delithiation terminates when a homogeneous Li concentration $C/C_{max} = 0.5$ within the particle is reached. Fig. 14(a) plots the radial distribution of Li concentration in the NMC secondary particle during delithiation. The outer shell is delithiated much sooner than the inner region and the chemical potential gradient of Li drives Li diffusion from the center toward the surface. Fig. 14(b) plots the contour profiles of Li concentration and delithiation-induced strain along the x-direction at the delithiation times $Dt/R^2 = 0.0048$, 0.024, and 0.24, respectively. At the early state of delithiation, the grains close to the surface experience a larger tensile strain owing to their low Li concentration. The mismatch strain from adjacent grains of different grain orientations can trigger intergranular cracks near the surface regime and drive the crack propagation toward the center of the NMC particle.

Intergranular cracks initiate and propagate when the energy release rate for crack growth exceeds the fracture resistance of the interface between primary particles. Fig. 15 plots the crack length as a function of the delithiation time for the NMC

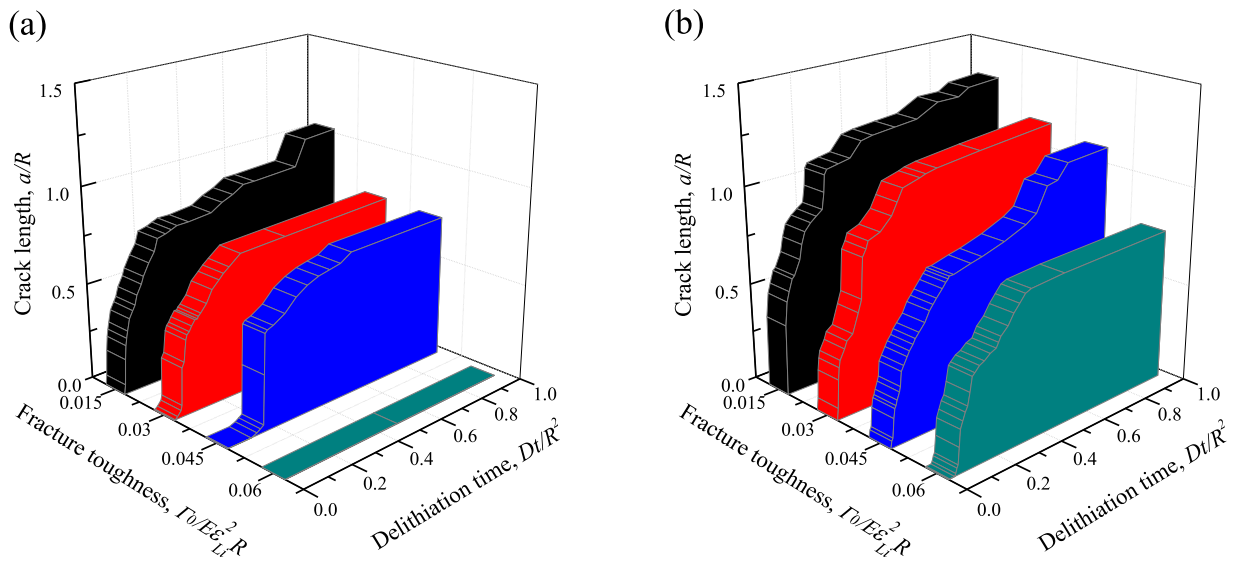

Fig. 16. 3D plots of intergranular crack length as a function of the delithiation time Dt/A^2 and the pristine fracture toughness of NMC $\Gamma_0/E\varepsilon_{Li}^2 L$ without (a) and with (b) considering the Li embrittlement effect.

particle of pristine interfacial fracture toughness $\Gamma_0/E\varepsilon_{Li}^2 L = 0.045$. The insets show the contour plots of the first principal stress at various delithiation times and their corresponding crack morphologies. The figures I–V show the crack patterns with the arrows indicating the crack growth path. Without considering the Li embrittlement effect, the NMC secondary particle has a constant interfacial fracture toughness upon Li reactions and the initiation of intergranular cracks is solely dependent on the development of tensile stress near the surface. Once an intergranular crack starts growing, the tensile stress and associated strain energy behind the crack tip are effectively released which prohibits initiation of another intergranular crack from the surface. The triggered crack propagates along the grain boundary and toward the center of the NMC particle as the field of mechanical stresses evolve upon delithiation, Fig. 15(a). The intergranular crack will eventually meet the joints of the grain boundaries which will force the crack to deflect. The deflection of crack requires a higher driving force for a continuous growth which retards or even stagnates the propagation of the intergranular crack in NMC. Overall, without considering the Li embrittlement effect, we observe that a single intergranular crack and its dynamics dominates the failure of NMC secondary particles. This morphology is somewhat different from the experimental observations in which the NMC particles are often disintegrated by multiple intergranular cracks and generation of several isolated clusters of primary particles (Ryu et al., 2018). This adds another motivation for us to examine the fracture behavior of NMC by including the Li embrittlement on the interfacial strength. Fig. 15(b) shows a similar plot of the evolution of the crack length upon Li extraction and snapshots of crack patterns and stress profiles at various times. At the stage I, an intergranular crack initiates from the surface and starts propagation. This intergranular crack initiates at an earlier time and propagates more quickly due to the Li embrittlement to the interface. After the initial crack growth, even though the tensile stress and the strain energy behind the crack tip are released, nucleation of new cracks elsewhere are still probable because the fracture resistance dramatically drops as the delithiation proceeds. When one intergranular crack encounters the grain joints that deflect the crack, other cracks are still in propagation, as seen in the snapshots from IV to V in Fig. 15(b). As a result, multiple cracks co-exist and co-evolve in the secondary particle and this fracture behavior is in good agreement with the experimental observations of the crack morphologies in NMC during the initial delithiation (Park et al., 2018; Ryu et al., 2018).

As previously discussed in Section 3.1, the corrosive fracture of electrodes is largely dependent on the fracture toughness of the pristine host material $\Gamma_0/E\varepsilon_{Li}^2 L$. Here we evaluate the effect of $\Gamma_0/E\varepsilon_{Li}^2 L$ on the intergranular crack of NMC secondary particles. We plot the length of the intergranular crack in a 3D configuration in terms of the delithiation time Dt/R^2 and the pristine fracture toughness $\Gamma_0/E\varepsilon_{Li}^2 L$, Fig. 16. In both cases with and without considering the Li embrittlement, the initial fracture toughness determines the time of crack initiation as well as the final crack length. In the case without Li embrittlement, no intergranular crack would occur for a high pristine fracture toughness $\Gamma_0/E\varepsilon_{Li}^2 L = 0.06$, while the same value of pristine fracture toughness is apparently insufficient to suppress the intergranular crack when considering the Li embrittlement effect. For $\Gamma_0/E\varepsilon_{Li}^2 L = 0.03$ and 0.045 in Fig. 16(a), the crack length remains a plateau in the later state of delithiation because the intergranular crack hits the grain joints and the driving force is not sufficient to overcome the resistance for crack deflection without Li embrittlement. In comparison, $\Gamma_0/E\varepsilon_{Li}^2 L = 0.045$ in Fig. 16(b) shows that, when the interfacial fracture toughness degrades in delithiation, the delithiation-induced mechanical stresses can cause the crack deflection and continuous growth. In general, whether the crack deflection will occur or not depends on the competition between the energy dissipation of crack deflection and Li embrittlement. If the energy dissipation of crack deflection is sufficiently small,

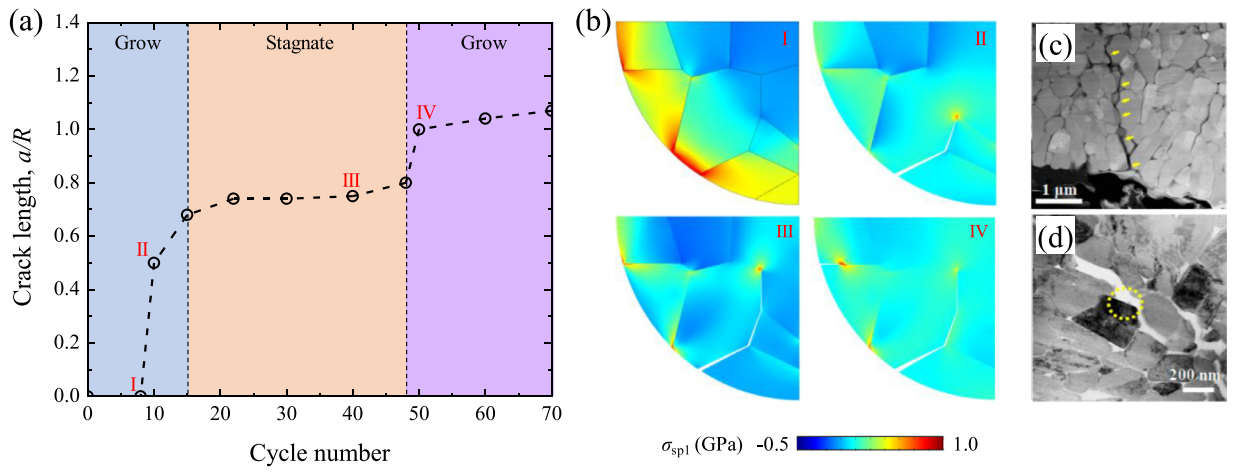

Fig. 17. (a) The growth of intergranular cracks in NMC secondary particles upon Li cycles. Crack stagnation is because of a larger driving force required to deflect the interfacial cracks at the joints of the grain boundaries. (b) The contour plots of the first principal stress at various cycle numbers and their corresponding crack morphologies. (c) SEM and (d) TEM images showing the intergranular cracks in NMC upon electrochemical cycles. Figures are reproduced from the work of Ryu et al. (2018).

crack deflection can still occur even though Li embrittlement is ignored, as indicated by the sudden increase of crack length for $\Gamma_0/E\varepsilon_{Li}^2 L = 0.015$ in Fig. 16(a).

3.2.2. Intergranular cracks in NMC upon Li cycles

We next model the dynamic evolution of corrosive intergranular cracks in NMC during Li cycles. Our previous experiments have shown that the electrochemical cycle deteriorates the interfacial strength of NMC particles due to the surface reconstruction and the accumulation of microscopic defects at the interface of the primary particles (Xu et al., 2017a). In the simulation of lithiation and delithiation cycles, we start with delithiation as described in Section 3.2.1, and once delithiation is finished, we perform lithiation by applying a chemical load $C_0/C_{\max} = 1$ on the surface of the NMC secondary particle. We repeat the delithiation and lithiation processes and set the interfacial fracture toughness as a function of the cycle number as shown in Fig. 13(d). We have ignored the variation of the fracture toughness within a cycle for the purpose of focusing on the dynamic fracture growth induced by the electrochemical cycles.

If Li embrittlement induced by the electrochemical cycles is not accounted, the fracture resistance remains constant as the Li cycle proceeds. In this case, even though a cyclic chemical load is applied to the NMC particle, the crack length will remain the same over cycles. In another word, either no crack forms if the interfacial fracture toughness is sufficiently high or the intergranular crack remains stagnation in the subsequent cycles if the crack stops growth in the first cycle. This scenario is contradictory to the typically observation in experiments that intergranular cracks in NMC steadily grows over cycle (Kim et al., 2016; Ryu et al., 2018). We attribute the fatigue-like damage accumulation in NMC upon electrochemical cycles to the Li embrittlement effect. Fig. 17(a) plots the evolution of intergranular cracks in NMC secondary particles where the crack length grows during Li cycles until the crack penetrates through the entire secondary particle. Specifically, the crack dynamics shows a “grow-stagnate-grow” behavior where the fast crack growth in the early cycles is induced by the Li embrittlement on the interfacial strength, the following crack stagnation is due to crack kinking at the joints of the grain boundaries, and the later stage of crack growth is because of the significant decrease of the fracture resistance after a large number of cycles that reduces the energy for crack deflection. To compare with the experimental observation of the crack morphology, a recent transmission electron microscopy (TEM) study (Kim et al., 2016) showed similar accumulation of damages in that most damages occurred within the first 10 cycles while the rate of damage accumulation in the following 10th to 100th cycle is much slower. In addition, Fig. 17(b) presents the contour plots of the first principal stress at various cycle numbers and their corresponding crack morphologies. The simulated crack morphologies caused by Li cycles agree well with the intergranular crack patterns in NMC observed by the scanning electron microscopy (SEM) and TEM, as shown in Fig. 17(c) and (d), respectively (Ryu et al., 2018).

4. Conclusions

We study the corrosive fracture of electrodes under concurrent mechanical and chemical load. Li acts like a corrosive species that deteriorates the mechanical strength of the host electrodes upon Li cycles. We implement the continuum theory of coupled diffusion and large deformation into finite element modeling. We investigate the fracture behavior that is dependent on the chemomechanical load, diffusion kinetics, Li embrittlement effect, and material properties. We examine in detail the competitive energy release rate and fracture resistance as crack grows during both Li insertion and extraction.

We construct the phase diagrams delineating the unstable, arrested, and delayed fracture zones in the variable space of material properties and the load conditions.

In the case of Li embrittlement during the insertion reaction, Li accumulation at the crack tip appends a local dilatational strain which reduces the stress field and thus the driving force for crack growth. Meanwhile, Li concentration at the crack tip also reduces the fracture toughness which promotes crack initiation. Crack propagates as a typical delayed fracture of the feature of "wait and go" – the "wait" depends on the Li transport and supply of Li at the crack tip, and the "go" depends on the Li embrittlement of the host. The pristine fracture toughness of the host material and the chemical load are the key parameters that determine the crack behavior. In the parametric studies, we reveal that the stress regulated Li diffusion promotes Li embrittlement through trapping Li at the crack tip, and a severer Li embrittlement effect facilitates delayed fracture.

For Li extraction induced material embrittlement which is typically observed in cathodes, we consider the driving force for crack growth entirely due to the delithiation induced volumetric contraction. The continuous Li extraction increases the energy release rate and reduces the fracture toughness of the host material which facilitates crack formation upon delithiation. Without an external mechanical load, the corrosive fracture shows two distinct behaviors: arrested and delayed fracture. In this case, the stress regulated Li diffusion provides a shielding effect at the crack tip which retards crack growth.

We apply the theory to model the intergranular fracture in NMC aggregated particles which constitutes the major mechanical degradation in NMC cathode materials. The structural decohesion is induced by the mismatch strain at the grain boundaries. The evolving interfacial strength at different states of charge and different cycle numbers is implemented in the numerical simulation. We model the corrosive behavior of intergranular cracks in NMC during delithiation and electrochemical cycles. Li embrittlement accelerates the initiation and growth of intergranular cracks in an NMC particle. Furthermore, Li embrittlement is a reason for the propagation of multiple intergranular cracks and crack deflection through the grain boundaries. The numerical modeling of crack growth and patterns agrees well with the experimental observations by recent TEM and SEM studies.

Acknowledgement

This work is supported by the National Science Foundation through the grants CMMI-1726392 and CBET-1603866.

References

Alam, M.Z., Das, D.K., 2009. Effect of cracking in diffusion aluminide coatings on their cyclic oxidation performance on Ti-based IMI-834 alloy. Corros. Sci. 51, 1405–1412.
Anand, L., 2012. A Cahn–Hilliard-type theory for species diffusion coupled with large elastic-plastic deformations. J. Mech. Phys. Solids 60, 1983–2002.
Anderson, T.L., 2017. Fracture Mechanics: Fundamentals and Applications. CRC Press.
Barnoush, A., Vehoff, H., 2010. Recent developments in the study of hydrogen embrittlement: hydrogen effect on dislocation nucleation. Acta Mater. 58, 5274–5285.
Berla, L.A., Lee, S.W., Cui, Y., Nix, W.D., 2015. Mechanical behavior of electrochemically lithiated silicon. J. Power Sources 273, 41–51.
Bhandakkar, T.K., Gao, H., 2010. Cohesive modeling of crack nucleation under diffusion induced stresses in a thin strip: implications on the critical size for flaw tolerant battery electrodes. Int. J. Solids Struct. 47, 1424–1434.
Bohn, E., Eckl, T., Kamlah, M., McMeeking, R., 2013. A model for lithium diffusion and stress generation in an intercalation storage particle with phase change. J. Electrochem. Soc. 160, A1638–A1652.
Bower, A.F., Chason, E., Guduru, P.R., Sheldon, B.W., 2015. A continuum model of deformation, transport and irreversible changes in atomic structure in amorphous lithium–silicon electrodes. Acta Mater. 98, 229–241.
Bower, A.F., Guduru, P.R., 2012. A simple finite element model of diffusion, finite deformation, plasticity and fracture in lithium ion insertion electrode materials. Model. Simul. Mater. Sci. Eng. 20, 045004.
Bower, A.F., Guduru, P.R., Sethuraman, V.A., 2011. A finite strain model of stress, diffusion, plastic flow, and electrochemical reactions in a lithium-ion half-cell. J. Mech. Phys. Solids 59, 804–828.
Brassart, L., Zhao, K., Suo, Z., 2013. Cyclic plasticity and shakedown in high-capacity electrodes of lithium-ion batteries. Int. J. Solids Struct. 50, 1120–1129.
Chan, C.K., Peng, H., Liu, G., McIlwrath, K., Zhang, X.F., Huggins, R.A., Cui, Y., 2008. High-performance lithium battery anodes using silicon nanowires. Nat. Nanotechnol 3, 31–35.
Christensen, J., Newman, J., 2006. Stress generation and fracture in lithium insertion materials. J. Solid State Electrochem. 10, 293–319.
Cui, S., Wei, Y., Liu, T., Deng, W., Hu, Z., Su, Y., Li, H., Li, M., Guo, H., Duan, Y., Wang, W., Rao, M., Zheng, J., Wang, X., Pan, F., 2016. Optimized temperature effect of Li-ion diffusion with layer distance in $Li(Ni_xMn_yCo_z)O_2$ cathode materials for high performance Li-ion battery. Adv. Energy Mater. 6, 1501309.
Elices, M., Guinea, G., Gomez, J., Planas, J., 2002. The cohesive zone model: advantages, limitations and challenges. Eng. Fract. Mech. 69, 137–163.
Evans, A.G., 1984. Fracture in ceramic materials. Toughening Mechanisms, Machining Damage, Shock. Noyes Publications, Department of Materials Science and Mineral Engineering, University of California, Park Ridge, Berkeley, NJ.
Gao, Y.F., Zhou, M., 2013. Coupled mechano-diffusional driving forces for fracture in electrode materials. J. Power Sources 230, 176–193.
Haftbaradaran, H., Qu, J., 2014. A path-independent integral for fracture of solids under combined electrochemical and mechanical loadings. J. Mech. Phys. Solids 71, 1–14.
Hao, X., Lin, X., Lu, W., Bartlett, B.M., 2014. Oxygen vacancies lead to loss of domain order, particle fracture, and rapid capacity fade in lithium manganospinel ($LiMn_2O_4$) batteries. ACS Appl. Mater. Interfaces 6, 10849–10857.
Hashin, Z., Rotem, A., 1973. A fatigue failure criterion for fiber reinforced materials. J. Compos. Mater. 7, 448–464.
Huang, X., Yang, H., Liang, W., Raju, M., Terrones, M., Crespi, V.H., van Duin, A.C.T., Zhang, S., 2013. Lithiation induced corrosive fracture in defective carbon nanotubes. Appl. Phys. Lett. 103, 153901.
Huggins, R.A., Nix, W.D., 2000. Decrepitation model for capacity loss during cycling of alloys in rechargeable electrochemical systems. Ionics (Kiel) 6, 57–63.
Jia, Z., Liu, W.K., 2016. Analytical model on stress-regulated lithiation kinetics and fracture of Si-C yolk-shell anodes for lithium-ion batteries. J. Electrochem. Soc. 163, A940–A946.
Kim, N.Y., Yim, T., Song, J.H., Yu, J.-S., Lee, Z., 2016. Microstructural study on degradation mechanism of layered $LiNi_{0.6}Co_{0.2}Mn_{0.2}O_2$ cathode materials by analytical transmission electron microscopy. J. Power Sources 307, 641–648.
Klinsmann, M., Rosato, D., Kamlah, M., McMeeking, R.M., 2016a. Modeling crack growth during Li extraction and insertion within the second half cycle. J. Power Sources 331, 32–42.

Klinsmann, M., Rosato, D., Kamlah, M., McMeeking, R.M., 2016b. Modeling crack growth during Li insertion in storage particles using a fracture phase field approach. J. Mech. Phys. Solids 92, 313–344.
Larché, F., Cahn, J.W., 1985. Overview no. 41 the interactions of composition and stress in crystalline solids. Acta Metall 33, 331–357.
Lee, S.W., Ryu, I., Nix, W.D., Cui, Y., 2015. Fracture of crystalline germanium during electrochemical lithium insertion. Extreme Mech. Lett. 2, 15–19.
Lin, X., Park, J., Liu, L., Lee, Y., Sastry, A., Lu, W., 2013. A comprehensive capacity fade model and analysis for Li-ion batteries. J. Electrochem. Soc. 160, A1701–A1710.
Liu, X.H., Zhong, L., Huang, S., Mao, S.X., Zhu, T., Huang, J.Y., 2012. Size-dependent fracture of silicon nanoparticles during lithiation. ACS Nano 6, 1522–1531.
Liu, Y., Zheng, H., Liu, X.H., Huang, S., Zhu, T., Wang, J., Kushima, A., Hudak, N.S., Huang, X., Zhang, S., 2011. Lithiation-induced embrittlement of multiwalled carbon nanotubes. ACS Nano 5, 7245–7253.
Maranchi, J.P., Hepp, A.F., Evans, A.G., Nuhfer, N.T., Kumta, P.N., 2006. Interfacial properties of the a-Si/Cu: active-inactive thin-film anode system for lithium-ion batteries. J. Electrochem. Soc. 153, A1246.
McDowell, M.T., Xia, S., Zhu, T., 2016. The mechanics of large-volume-change transformations in high-capacity battery materials. Extreme Mech. Lett. 9, 480–494.
Molins, R., Hochstetter, G., Chassaigne, J., Andrieu, E., 1997. Oxidation effects on the fatigue crack growth behaviour of alloy 718 at high temperature. Acta Mater. 45, 663–674.
Mu, L., Lin, R., Xu, R., Han, L., Xia, S., Sokaras, D., Steiner, J.D., Weng, T.C., Nordlund, D., Doeff, M.M., Liu, Y., Zhao, K., Xin, H.L., Lin, F., 2018. Oxygen release induced chemomechanical breakdown of layered cathode materials. Nano Lett. 18, 3241–3249.
Mughal, M.Z., Moscatelli, R., Amanieu, H.Y., Sebastiani, M., 2016. Effect of lithiation on micro-scale fracture toughness of LixMn2O4 cathode. Scr. Mater. 116, 62–66.
Ning, G., Haran, B., Popov, B.N., 2003. Capacity fade study of lithium-ion batteries cycled at high discharge rates. J. Power Sources 117, 160–169.
Palacin, M.R., de Guibert, A., 2016. Why do batteries fail? Science 351, 1253292.
Park, S.Y., Baek, W.J., Lee, S.Y., Seo, J.A., Kang, Y.-S., Koh, M., Kim, S.H., 2018. Probing electrical degradation of cathode materials for lithium-ion batteries with nanoscale resolution. Nano Energy 49, 1–6.
Pharr, M., Choi, Y.S., Lee, D., Oh, K.H., Vlassak, J.J., 2016. Measurements of stress and fracture in germanium electrodes of lithium-ion batteries during electrochemical lithiation and delithiation. J. Power Sources 304, 164–169.
Pharr, M., Suo, Z., Vlassak, J.J., 2013. Measurements of the fracture energy of lithiated silicon electrodes of Li-ion batteries. Nano Lett. 13, 5570–5577.
Rice, J.R., 1968. A path independent integral and the approximate analysis of strain concentration by notches and cracks. J. Appl. Mech. 35, 379–386.
Roe, K., Siegmund, T., 2003. An irreversible cohesive zone model for interface fatigue crack growth simulation. Eng. Fract. Mech. 70, 209–232.
Ryu, H.-H., Park, K.-J., Yoon, C.S., Sun, Y.-K., 2018. Capacity fading of Ni-Rich $Li[Ni_xCo_yMn_{1-x-y}]O_2$ $(0.6\leq x\leq 0.95)$ cathodes for high-energy-density lithium-ion batteries: Bulk or surface degradation? Chem. Mat. 30, 1155–1163.
Ryu, I., Choi, J.W., Cui, Y., Nix, W.D., 2011. Size-dependent fracture of Si nanowire battery anodes. J. Mech. Phys. Solids 59, 1717–1730.
Sarkar, A., Shrotriya, P., Chandra, A., 2017. Fracture modeling of lithium-silicon battery based on variable elastic moduli. J. Electrochem. Soc. 164, E3606–E3612.
Shih, C., Moran, B., Nakamura, T., 1986. Energy release rate along a three-dimensional crack front in a thermally stressed body. Int. J. Fract. 30, 79–102.
Sofronis, P., McMeeking, R.M., 1989. Numerical analysis of hydrogen transport near a blunting crack tip. J. Mech. Phys. Solids 37, 317–350.
Sun, H., Xin, G., Hu, T., Yu, M., Shao, D., Sun, X., Lian, J., 2014. High-rate lithiation-induced reactivation of mesoporous hollow spheres for long-lived lithium-ion batteries. Nat. Commun. 5, 4526.
Sun, H., Zhao, K., 2017. Electronic structure and comparative properties of $LiNi_xMn_yCo_zO_2$ cathode materials. J. Phys. Chem. C 121, 6002–6010.
Swallow, J.G., Woodford, W.H., McGrogan, F.P., Ferralis, N., Chiang, Y.M., Van Vliet, K.J., 2014. Effect of electrochemical charging on elastoplastic properties and fracture toughness of Li_xCoO_2. J. Electrochem. Soc. 161, F3084–F3090.
Tarascon, J.-M., Armand, M., 2012. Issues and Challenges Facing Rechargeable Lithium Batteries, Materials for Sustainable Energy. Macmillan Publishers Ltd., UK, pp. 171–179.
Vasconcelos, L.S., Xu, R., Li, J., Zhao, K., 2016. Grid indentation analysis of mechanical properties of composite electrodes in Li-ion batteries. Extreme Mech. Lett. 9, 495–502.
Vasconcelos, L.S., Xu, R., Zhao, K., 2017. Operando nanoindentation: a new platform to measure the mechanical properties of electrodes during electrochemical reactions. J. Electrochem. Soc. 164, A3840–A3847.
Wang, H., Jang, Y.I., Huang, B., Sadoway, D.R., Chiang, Y.M., 1999. TEM study of electrochemical cycling-induced damage and disorder in $LiCoO_2$ cathodes for rechargeable lithium batteries. J. Electrochem. Soc. 146, 473–480.
Woodford, W.H., Chiang, Y.-M., Carter, W.C., 2010. “Electrochemical shock” of intercalation electrodes: a fracture mechanics analysis. J. Electrochem. Soc 157, A1052.
Xu, R., Sun, H., Vasconcelos, L.S., Zhao, K., 2017a. Mechanical and structural degradation of $LiNi_xMn_yCo_zO_2$ cathode in Li-ion batteries: an experimental study. J. Electrochem. Soc. 164, A3333–A3341.
Xu, R., Vasconcelos, L.S., Shi, J., Li, J., Zhao, K., 2017b. Disintegration of meatball electrodes for $LiNi_xMn_yCo_zO_2$ cathode materials. Exp. Mech. 58, 549–559.
Xu, R., Vasconcelos, L.S., Zhao, K., 2016. Computational analysis of chemomechanical behaviors of composite electrodes in Li-ion batteries. J. Mater. Res. 31, 2715–2727.
Xu, R., Zhao, K., 2016a. Electrochemomechanics of electrodes in Li-ion batteries: A review. J. Electrochem. Energy Convers. 13, 030803.
Xu, R., Zhao, K., 2016b. Mechanical interactions regulated kinetics and morphology of composite electrodes in Li-ion batteries. Extreme Mech. Lett. 8, 13–21.
Yan, P., Zheng, J., Gu, M., Xiao, J., Zhang, J.G., Wang, C.M., 2017. Intragranular cracking as a critical barrier for high-voltage usage of layer-structured cathode for lithium-ion batteries. Nat. Commun. 8, 14101.
Yan, P., Zheng, J., Lv, D., Wei, Y., Zheng, J., Wang, Z., Kuppan, S., Yu, J., Luo, L., Edwards, D., 2015. Atomic-resolution visualization of distinctive chemical mixing behavior of Ni, Co, and Mn with Li in layered lithium transition-metal oxide cathode materials. Chem. Mat. 27, 5393–5401.
Yang, F., Liu, B., Fang, D.-N., 2011. Interplay between fracture and diffusion behaviors: Modeling and phase field computation. Comput. Mater. Sci. 50, 2554–2560.
Yang, H., Huang, X., Liang, W., van Duin, A.C.T., Raju, M., Zhang, S., 2013. Self-weakening in lithiated graphene electrodes. Chem. Phys. Lett. 563, 58–62.
Zhang, M., Qu, J., Rice, J.R., 2017a. Path independent integrals in equilibrium electro-chemo-elasticity. J. Mech. Phys. Solids 107, 525–541.
Zhang, S., 2017. Chemomechanical modeling of lithiation-induced failure in high-volume-change electrode materials for lithium ion batteries. NPJ Comput. Mater. 3, 7.
Zhang, S., Zhao, K., Zhu, T., Li, J., 2017b. Electrochemomechanical degradation of high-capacity battery electrode materials. Prog. Mater. Sci. 89, 479–521.
Zhang, X., Shyy, W., Marie Sastry, A., 2007. Numerical Simulation of Intercalation-Induced Stress in Li-Ion Battery Electrode Particles. J. Electrochem. Soc. 154, A910.
Zhao, K., Cui, Y., 2016. Understanding the role of mechanics in energy materials: A perspective. Extreme Mech. Lett. 9, 347–352.
Zhao, K., Pharr, M., Cai, S., Vlassak, J.J., Suo, Z., 2011. Large plastic deformation in high-capacity lithium-ion batteries caused by charge and discharge. J. Am. Ceram. Soc. 94.
Zhao, K., Pharr, M., Hartle, L., Vlassak, J.J., Suo, Z., 2012. Fracture and debonding in lithium-ion batteries with electrodes of hollow core-shell nanostructures. J. Power Sources 218, 6–14.
Zhao, K., Pharr, M., Vlassak, J.J., Suo, Z., 2010. Fracture of electrodes in lithium-ion batteries caused by fast charging. J. Appl. Phys. 108, 073517.